

**2-FLUID MODELING OF MAGNETIZED PLASMA
TRANSPORT IN AXISYMMETRIC DOMAINS
WITH GALERKIN FINITE ELEMENTS**

Roberto Zanino

Max-Planck-Institut für Plasmaphysik, D-8046 Garching
Dipartimento di Energetica, Politecnico, I-10129 Torino

IPP 5/43

September 1991



MAX-PLANCK-INSTITUT FÜR PLASMAPHYSIK

8046 GARCHING BEI MÜNCHEN

MAX-PLANCK-INSTITUT FÜR PLASMAPHYSIK

GARCHING BEI MÜNCHEN

2-FLUID MODELING OF MAGNETIZED PLASMA TRANSPORT IN AXISYMMETRIC DOMAINS WITH GALERKIN FINITE ELEMENTS

Roberto Zanino

Max-Planck-Institut für Plasmaphysik, D-8046 Garching
Dipartimento di Energetica, Politecnico, I-10129 Torino

ABSTRACT

IPP 5/43

September 1991

We present a Galerkin finite element code for time dependent transport modeling of a pure 2-fluid magnetized plasma in an axisymmetric domain. The code is intended to be used as a basis for finite element modeling of the tokamak scrape-off layer. The collisional dynamics along magnetic field lines is taken into account, a simple diffusive Ansatz is used for the transport across magnetic surfaces, and diamagnetic flows are neglected. In principle any magnetic field and first wall geometry is allowed, this flexibility being the main rationale for the use of finite elements. Results for an extensive set of test cases in simple geometry are discussed.

*Die nachstehende Arbeit wurde im Rahmen des Vertrages zwischen dem
Max-Planck-Institut für Plasmaphysik und der Europäischen Atomgemeinschaft über
die Zusammenarbeit auf dem Gebiete der Plasmaphysik durchgeführt.*

ABSTRACT

We present a Galerkin finite element code for time dependent transport modeling of a pure 2-fluid magnetized plasma in an axisymmetric domain. The code is intended to be used as a basis for finite element modeling of the tokamak scrape-off layer. The collisional dynamics along magnetic field lines is taken into account, a simple diffusive Ansatz is used for the transport across magnetic surfaces, and diamagnetic flows are neglected. In principle any magnetic field and first wall geometry is allowed, this flexibility being the main rationale for the use of finite elements. Results for an extensive set of test cases in simple geometry are discussed.

Introduction

Finite elements should provide a more natural and flexible method than finite differences (see, e.g., [1]) for two-dimensional fluid modeling of the tokamak scrape-off layer (SOL). Among others they could present the advantage of:

- 1) an adequate treatment of the region near the targets, when the poloidal magnetic field lines are very inclined to them; this will be the case for the divertor plates in a fusion reactor (in order to spread the power on a larger surface) and anyway for a limiter (where at least at one point the field is tangent to the solid surface). For SOL modeling one natural coordinate is always tangent to the poloidal magnetic field line, due to transport anisotropy and toroidal symmetry, whereas the solution is expected to develop large gradients only within a short distance from the target, where sources can be large: then problems arise with finite differences in an orthogonal mesh when the target does not lay orthogonal to the poloidal field, and this requires either many useless points, or possibly inaccurate approximation of the target in a stair-like fashion, or else recurring to a cumbersome non-orthogonal coordinate system;

- 2) a treatment of the typically non simply connected domain which does not require, as is the case with finite differences, cuts and artificial boundary conditions;

- 3) a capability to adapt to different geometries of the edge region, particularly in the design phase of a machine.

In this paper, the fourth of a series [2-4], we present a finite element code based on the Galerkin method, for time-dependent two-dimensional two-fluid description of a pure magnetized plasma. The model contains detailed collisional physics [5] in the direction along field lines, and the simplest diffusive Ansatz for the transport of particles momentum and energy in the direction perpendicular to the magnetic surfaces.

Although the code is written in such a way as to be applicable to any given combination of magnetic and target geometry, only the simplest rectangular geometry will be dealt with in the examples presented here, and the coupling to a Grad-Shafranov solver for the equilibrium will be considered in a forthcoming work.

The paper is organized as follows: in Section 1 the model equations are presented; in Section 2 they are rewritten in weighted residual form and boundary conditions are discussed; in Section 3 we briefly review linearization of the equations, Galerkin formulation and time marching procedure; in Section 4 results are presented for an extensive set of test cases in simple geometry, for which the exact steady state solution can be easily constructed analytically; in Section 5, finally, we summarize our conclusions and discuss some of the questions to be addressed in future work.

1. Model equations

We consider a pure (electrons and singly charged ions) magnetized plasma, sufficiently collisional to make a fluid description meaningful, but still allowing for possibly different ion and electron temperatures, $T_e \neq T_i$.

The plasma is assumed to be quasineutral, i.e., for the particle densities one has

$$n_e = n_i \equiv n \quad (1)$$

and we assume to have no electric currents flowing in the plasma

$$\mathbf{V}_e = \mathbf{V}_i \equiv \mathbf{V} \quad (2)$$

(see [6] for a 1-D analysis of the case with currents).

Rewriting the classical Braginskii equations [5] in form of conservation laws (at least partly), and adding sources one has (the "t" subscript indicates a partial derivative with respect to time):

the continuity equation (mass balance)

$$\rho_t = -\nabla \cdot (\rho \mathbf{V}) + S^m; \quad (3)$$

the total momentum balance

$$\Gamma_t = -\nabla \cdot [\rho \mathbf{V} \mathbf{V} + (p_e + p_i) \mathbf{I} + \Pi_i] + \mathbf{S}^P; \quad (4)$$

the electron energy balance

$$\frac{3}{2}(p_e)_t = -\nabla \cdot \left(\frac{5}{2} n T_e \mathbf{V} + \mathbf{q}_e \right) + \mathbf{V} \cdot (\nabla p_e - \mathbf{S}_e^P) + Q_e + S_e^E; \quad (5)$$

the total energy balance

$$\mathcal{E}_t = -\nabla \cdot \left(\frac{5}{2} n T_e \mathbf{V} + \frac{5}{2} n T_i \mathbf{V} + \frac{1}{2} \rho V^2 \mathbf{V} + \Pi_i \cdot \mathbf{V} + \mathbf{q}_e + \mathbf{q}_i \right) + S^E. \quad (6)$$

Mass density, mass flow, electron pressure and total energy density define the vector of unknowns as

$$\begin{aligned} \mathbf{u} &= [\rho, \Gamma, p_e, \mathcal{E}] \\ &\equiv [m_i n, \rho \mathbf{V}, n T_e, \left(\frac{3}{2} n T_e + \frac{3}{2} n T_i + \frac{1}{2} \rho V^2 \right)] \end{aligned} \quad (7)$$

where m_i is the ion mass; the right-hand sides in (3)-(6) will obviously have to be expressed as functions of \mathbf{u} .

Due to interactions with (e.g., recycling) neutral particles, sources and sinks act on the plasma: a mass source S^m , an electron and a total momentum source S_e^P and \mathbf{S}^P , an electron and a total energy source S_e^E and S^E .

In (4) \mathbf{I} is the identity matrix, Π_i is the ion viscous stress tensor; the electron mass and the electron viscous stress tensor have been neglected.

In (5) \mathbf{q}_e is the electron heat flux. The second term on the right-hand side represents the work done by the electric field; notice that due to this term, i.e., due to the electric coupling between the electron and the ion fluids, it is generally impossible to write the whole system in conservation form; electron viscosity would also enter here. The third term on the right-hand side represents the energy interchange between ions and electrons due to their different temperatures [5]

$$Q_e = 3 \frac{m_e}{m_i} \frac{n}{\tau_e} (T_i - T_e) \quad (5a)$$

where m_e is the electron mass and $\tau_e \propto T_e^{3/2}/n$ is the classical electron-ion collision time.

In (6), finally, also the ion heat flux contribution q_i is taken into account.

Constitutive relations will be needed for the heat fluxes and the viscous stress tensor.

In this paper we shall consider the solution of the previous system, in a three-dimensional axisymmetric domain \mathcal{D} as shown in Fig.1. Let us define Ω as the intersection of \mathcal{D} with a poloidal plane (i.e., a plane passing through the axis of symmetry); at each $x \in \Omega$ we assume given a unit vector b tangent to the magnetic field line at x , and we define b_θ the projection of b on Ω , e_θ the unit vector along b_θ , and e_ψ the unit vector obtained rotating e_θ by 90 degrees clockwise on Ω ; finally, $e_\phi = e_\psi \times e_\theta$, and $e_\phi \cdot \nabla a = 0$ for any scalar a , expressing axisymmetry.

Clearly, in the most general case the flow fields will have three independent components; in the case of the mass flow, e.g., their evolution would be described by the corresponding component of (4). However, in the present paper we adopt a customary [1] simplified picture:

1) We assume the $b \times e_\psi$ component of the flow (tangent to the magnetic surface but orthogonal to the field) to vanish, i.e., we neglect diamagnetic flows. Qualitatively this can be justified observing that for a description of the SOL one needs in first approximation only two mechanisms: one for (fast) transport to the target, and one for (slow) transport through magnetic surfaces.

2) Since, as is well known, there is no rigorous theoretical model for transport across magnetic surfaces, we make for all radial (\equiv along e_ψ) fluxes a simple diffusive Ansatz, assuming known *anomalous* transport coefficients.

Constitutive relations

For the mass flow field we assume

$$\Gamma = \Gamma_{\parallel} b + \Gamma_{\psi} e_{\psi} \quad (8)$$

and

$$\Gamma_{\psi} = -D_{an} \frac{\partial \rho}{\partial \psi} \quad (9)$$

where $\partial/\partial\psi \equiv \mathbf{e}_\psi \cdot \nabla$. The evolution of Γ_\parallel will be given by the \mathbf{b} component of the weak form of (4), see next Section.

For the stress tensor (viscous momentum flux) we neglect the contributions from gyroviscosity and classical perpendicular viscosity, and assume

$$\Pi_i = -\eta_0^i \frac{\partial V_\parallel}{\partial \theta} b_\theta^2 (\mathbf{e}_\theta \mathbf{e}_\phi + \mathbf{e}_\phi \mathbf{e}_\theta) - \rho \eta_{an} \frac{\partial V_\parallel}{\partial \psi} (\mathbf{e}_\psi \mathbf{e}_\phi + \mathbf{e}_\phi \mathbf{e}_\psi) \quad (10)$$

where $\eta_0^i \propto T_i^{5/2}$ is the classical ion parallel viscosity [5], $\partial/\partial\theta \equiv \mathbf{e}_\theta \cdot \nabla$. Notice that [7], assuming (8) and $b_\theta^2 \ll 1$: 1) the full contribution of η_0 to the parallel momentum balance would come from $\Pi_0^\parallel = -b_\theta \eta_0 A_0$ where $A_0 \equiv \frac{2}{3} b_\theta (2 \frac{\partial V_\parallel}{\partial \theta} + \frac{1}{B} \frac{\partial B}{\partial \theta} V_\parallel)$, whereas we use $A_0 \approx b_\theta \frac{\partial V_\parallel}{\partial \theta}$; 2) the full contribution of η_0 to the total energy balance would include $V_\psi \Pi_{\psi\psi} \frac{\partial \lambda}{\partial \psi}$, see (16), with $\Pi_{\psi\psi} = \frac{1}{2} \eta_0 A_0$, which we neglect (where the particle source is negligible this contribution would be of the same order of that from $\Pi_{\phi\theta}$). Therefore, (10) contains the correct order of magnitude of the η_0 contribution.

For the heat fluxes ($j=i,e$) we neglect the contributions from gyro- and classical perpendicular heat conductivity, and assume

$$\mathbf{q}_j = -\kappa_\parallel^j (\mathbf{b} \cdot \nabla T_j) \mathbf{b} - n \chi_{an}^j (\mathbf{e}_\psi \cdot \nabla T_j) \mathbf{e}_\psi \quad (11)$$

where $\kappa_\parallel^j \propto T_j^{5/2}$ is the classical parallel heat conductivity [5]; in the following we will neglect $\kappa_\parallel^i \ll \kappa_\parallel^e$.

2. Weighted residuals formulation and boundary conditions

One of the reasons to write the equations in our system in conservative form is that application of Green's lemma (multidimensional integration by parts) to the weighted residual formulation leads to: 1) much easier evaluation of several terms (e.g., inertial, viscous, etc.); 2) natural boundary conditions.

To obtain the weighted residual formulation of (3)-(6),(9) we multiply each scalar equation by a respective test function, then integrate over \mathcal{D} , and use Green's lemma in the usual way

to lower by one order the highest (second) derivatives appearing in the system. Indicating by \mathbf{n} the outward normal to the boundary $\partial\Omega$ of Ω we are led to the system:

$$\langle \rho_t \lambda^\rho \rangle = - \int_{\partial\Omega, \text{in}} (\Gamma \cdot \mathbf{n}) \lambda^\rho R \, d\ell - \int_{\partial\Omega, \text{out}} (\Gamma \cdot \mathbf{n}) \lambda^\rho R \, d\ell + \langle \Gamma \cdot \nabla \lambda^\rho \rangle + \langle S^m \lambda^\rho \rangle \quad (12)$$

expressing mass conservation in weak form;

$$\begin{aligned} \langle (\Gamma_{\parallel})_t \lambda^{\parallel} \rangle = & - \oint_{\partial\Omega} (\mathbf{b} \cdot \Gamma^P \cdot \mathbf{n}) \lambda^{\parallel} R \, d\ell + \langle \frac{\Gamma_{\parallel}}{\rho} \Gamma \cdot \nabla \lambda^{\parallel} \rangle + \langle (\frac{2}{3} \mathcal{E} - \frac{1}{3} \frac{\Gamma^2}{\rho}) \mathbf{b} \cdot \nabla \lambda^{\parallel} \rangle - \\ & \langle b_\phi b_\theta^2 \eta_0^i \frac{\partial}{\partial \theta} (\Gamma_{\parallel} / \rho) \frac{\partial \lambda^{\parallel}}{\partial \theta} \rangle - \langle b_\phi \rho \eta_{\text{an}} \frac{\partial}{\partial \psi} (\Gamma_{\parallel} / \rho) \frac{\partial \lambda^{\parallel}}{\partial \psi} \rangle + \langle \mathbf{b} \cdot \mathbf{S}^P \lambda^{\parallel} \rangle \end{aligned} \quad (13)$$

expressing parallel momentum conservation in weak form;

$$\langle \Gamma_\psi \lambda^\psi \rangle = - \langle D_{\text{an}} \frac{\partial \rho}{\partial \psi} \lambda^\psi \rangle \quad (14)$$

expressing the diffusive Ansatz on the radial mass flow in weak form (notice that we keep (14) as a separate equation, notwithstanding its trivial form, in view of future developments when a more complex treatment of radial transport will be included);

$$\begin{aligned} \langle (p_e)_t \lambda^e \rangle = & - \frac{2}{3} \oint_{\partial\Omega} (\Gamma_e^E \cdot \mathbf{n}) \lambda^e R \, d\ell + \frac{5}{3} \langle \frac{p_e}{\rho} \Gamma \cdot \nabla \lambda^e \rangle - \\ & \frac{2}{3} m_i \langle b_\theta^2 \kappa_\parallel^e \frac{\partial}{\partial \theta} (p_e / \rho) \frac{\partial \lambda^e}{\partial \theta} \rangle - \frac{2}{3} \langle \rho \chi_{\text{an}}^e \frac{\partial}{\partial \psi} (p_e / \rho) \frac{\partial \lambda^e}{\partial \psi} \rangle + \\ & \frac{2}{3} \langle \frac{1}{\rho} \Gamma \cdot (\nabla p_e) \lambda^e \rangle + \frac{4}{3} \frac{m_e}{m_i} \langle \frac{1}{\tau_e} (\mathcal{E} - 3p_e - \frac{1}{2} \frac{\Gamma^2}{\rho}) \lambda^e \rangle - \frac{2}{3} \langle \frac{1}{\rho} \Gamma \cdot \mathbf{S}_e^P \lambda^e \rangle + \frac{2}{3} \langle S_e^E \lambda^e \rangle \end{aligned} \quad (15)$$

expressing the electron energy balance in weak form;

$$\begin{aligned} \langle \mathcal{E}_t \lambda^E \rangle = & - \oint_{\partial\Omega} (\Gamma^E \cdot \mathbf{n}) \lambda^E R \, d\ell + \frac{5}{3} \langle \frac{\mathcal{E}}{\rho} \Gamma \cdot \nabla \lambda^E \rangle - \frac{1}{3} \langle \frac{\Gamma^2}{\rho^2} \Gamma \cdot \nabla \lambda^E \rangle - \\ & \langle b_\phi b_\theta^2 \eta_0^i \frac{\Gamma_{\parallel}}{\rho} \frac{\partial}{\partial \theta} (\Gamma_{\parallel} / \rho) \frac{\partial \lambda^E}{\partial \theta} \rangle - \langle b_\phi \eta_{\text{an}} \Gamma_{\parallel} \frac{\partial}{\partial \psi} (\Gamma_{\parallel} / \rho) \frac{\partial \lambda^E}{\partial \psi} \rangle - \\ & m_i \langle b_\theta^2 \kappa_\parallel^e \frac{\partial}{\partial \theta} (p_e / \rho) \frac{\partial \lambda^E}{\partial \theta} \rangle - \langle \rho \chi_{\text{an}}^e \frac{\partial}{\partial \psi} (p_e / \rho) \frac{\partial \lambda^E}{\partial \psi} \rangle - \\ & \frac{2}{3} \langle \rho \chi_{\text{an}}^i \frac{\partial}{\partial \psi} [(\mathcal{E} - \frac{3}{2} p_e - \frac{1}{2} \frac{\Gamma^2}{\rho}) \frac{1}{\rho}] \frac{\partial \lambda^E}{\partial \psi} \rangle + \langle S^E \lambda^E \rangle \end{aligned} \quad (16)$$

expressing the total energy balance in weak form. In (12)-(16) $\langle f \rangle \equiv \int_{\Omega} f R \, d\Omega$, R is the distance (major radius) of $d\Omega$ from the symmetry axis, $d\ell$ is the length element on $\partial\Omega$, and $b_\phi = \sqrt{1 - b_\theta^2}$. The obvious definitions, coming from (4)-(6), were used:

(tensor) momentum flux

$$\Gamma^P \equiv \rho \mathbf{V} \mathbf{V} + (p_e + p_i) \mathbf{I} + \Pi_i; \quad (17)$$

electron energy flux

$$\Gamma_e^E \equiv \frac{5}{2} n T_e \mathbf{V} + \mathbf{q}_e; \quad (18)$$

total energy flux

$$\Gamma^E \equiv \frac{5}{2} n T_e \mathbf{V} + \frac{5}{2} n T_i \mathbf{V} + \frac{1}{2} \rho V^2 \mathbf{V} + \Pi_i \cdot \mathbf{V} + \mathbf{q}_e + \mathbf{q}_i. \quad (19)$$

Two types of boundary conditions are foreseen in the code:

1) Dirichlet (essential) boundary conditions, requiring assignment of some components of \mathbf{u} as given space functions on portions of $\partial\Omega$:

$$\sum_{k=1}^5 \alpha_{jk}(\mathbf{x}) u_k(\mathbf{x}, t) = \bar{u}_j(\mathbf{x}) \quad j = 1, 2, 4, 5 \quad \mathbf{x} \in \partial\Omega_{jD}; \quad (20)$$

2) Robin (natural) boundary conditions, requiring assignment of some components of

$$\mathbf{G} \equiv [\Gamma \cdot \mathbf{n}, \mathbf{b} \cdot \Gamma^P \cdot \mathbf{n}, 0, \Gamma_e^E \cdot \mathbf{n}, \Gamma^E \cdot \mathbf{n}]$$

as a linear combination of the components of \mathbf{u} , on other portions of $\partial\Omega$:

$$G_j(\mathbf{x}, t) = \sum_{k=1}^5 \beta_{jk}(\mathbf{x}) u_k(\mathbf{x}, t) + \gamma_j(\mathbf{x}) \quad j = 1, 2, 4, 5 \quad \mathbf{x} \in \partial\Omega_{jR}. \quad (21)$$

Since the continuity equation is hyperbolic (at least "along \mathbf{e}_θ ") only the inflow ("in") boundary fluxes can be assigned, whereas at the outflow ("out") boundary the corresponding line integral needs be discretized as all the other terms. Notice, however, that when $\Gamma_\psi \mathbf{e}_\psi \cdot \mathbf{n} > 0$ at some point on the boundary, there a boundary condition is needed because due to the diffusive Ansatz (9) the continuity equation is in effect parabolic "along \mathbf{e}_ψ ".

Since (3)-(6) are parabolic, boundary conditions for (13),(15),(16) are needed everywhere on $\partial\Omega$.

3. Linearization, Galerkin formulation, and time marching procedure

The system (12)-(16) can be formally rewritten as

$$\mathcal{M}u_t = a(u). \quad (22)$$

Time marching of (22) towards steady state is accomplished by the theta-method (below, μ indicates the parameter, to avoid confusion with the poloidal coordinate): the time derivatives are approximated as finite differences, and the right-hand side is evaluated as a convex combination of its values at time "k" and time "k+1":

$$\mathcal{M} \frac{u^{k+1} - u^k}{t^{k+1} - t^k} = (1 - \mu)a(u^k) + \mu a(u^{k+1}) \quad (23)$$

where $u^k \equiv u(t^k)$; therefore, both explicit ($\mu = 0$) and fully implicit ($\mu = 1$) schemes are included, as well as a combination of the two ($0 < \mu < 1$).

Equations (23) are linearized by a single step of Newton's iteration, leading to:

$$\left(\frac{\mathcal{M}}{t^{k+1} - t^k} - \mu \mathcal{J} \right) u^{k+1} = \left(\frac{\mathcal{M}}{t^{k+1} - t^k} - \mu \mathcal{J} \right) u^k + a(u^k) \quad (24)$$

where $\mathcal{J} \equiv \partial a / \partial u$ at $u = u^k$ is the Jacobian matrix. Generally, also the actual boundary conditions need be similarly linearized, in order to put them in the form (20)-(21); in that case $\alpha_{jk}, \bar{u}_j, \beta_{jk}, \gamma_j$ at each time step can also depend on the value of u at the previous time step. (Of the nonlinearities in the transport coefficients only $\kappa_{||}^e$ has been linearized, whereas η_0^i and τ_e are treated explicitly in time).

To discretize (24) in space we first introduce a triangulation of Ω ; we then take $\lambda^p = \lambda^|| = \lambda^\psi = \lambda^e = \lambda^E = \lambda$, and express each of the u components as a function of the λ 's (Galerkin method): for the present time we have implemented in the code the case λ

equal to the linear hat function of value 1 at node (\equiv vertex) "i", and vanishing at all neighbouring nodes. If there are "N" nodes in the mesh we obtain therefore from (20), (21) and (24) a linear system of $5N$ equations for the value of \mathbf{u} at the nodes, which is solved at each time step by the GMRES iterative method (see [4]).

The time step $(\Delta t)_{k+1} \equiv t^{k+1} - t^k$ is adapted in a way strictly similar to that discussed in [4]. In cases when one is interested in the steady state only, a local time step can be used to speedup the computation. Additionally, the timestep can also be different in different equations. When the time step is both local and equation dependent, $(\Delta t)_{k+2}$ for the evolution of, say, ρ at node i , will depend on the value of $|\rho^{k+1}(\mathbf{x}_i) - \rho^k(\mathbf{x}_i)|/\rho^{k+1}(\mathbf{x}_i)$; the time step used in the computation of the elemental matrix is the minimum among the respective time steps at the vertexes of the triangle.

4. Results for test cases in simple geometry

We have performed several tests of the code, all concerned with the relaxation to different exactly computable steady states. We assume the steady state to be reached when the absolute value of the maximum relative variation of ρ , p_e , \mathcal{E} during the last time step is below a given tolerance ζ (typically 10^{-3}), and $\Delta t = \Delta t_{max} \sim L_Z \sqrt{m_i/\bar{T}}$, where L_Z is the connection length (see below) and $\bar{T} = 10\text{eV}$. The same Δt was used in all equations and uniform in Ω , with the fully implicit scheme.

Due to limitations (see [4]) of the present version of the unstructured mesh generator available to us, we restricted ourselves to a simple domain and magnetic field geometry. We considered as domain Ω the rectangle $R_0 \leq R \leq R_0 + L_R$ and $0 \leq Z \leq L_Z$, as shown in Fig.2. The poloidal magnetic field is directed vertically (i.e., along \mathbf{e}_Z) and we took for simplicity $b_\theta = 0.1$ everywhere. Notice that the mesh shown in the following Figures, for the purpose of easy representation, results from a contraction by a factor 10^2 along \mathbf{e}_Z , of the mesh actually used in the computation.

Anomalous transport coefficients are taken all equal and of the order of $1m^2s^{-1}$. Parallel transport coefficients are classical except for an enhancement by a factor 10 of η_0^i (see below).

In a first series of tests no sources act on the system.

As boundary conditions we assume: $R = R_0$, $Z = 0$ and $Z = L_Z$ as ideally adiabatic, i.e., the normal components of all the flows are set to zero in the boundary integrals; the parallel particle flow is set to zero as a Dirichlet condition at $Z = 0$ and $Z = L_Z$, and it is free at $R = R_0$; at $R = R_0 + L_R$ we impose the Dirichlet boundary conditions $\rho = \bar{\rho}$, $\Gamma_{\parallel} = 0$, $p_e = \bar{p}_e$, $\mathcal{E} = \bar{\mathcal{E}}$.

We begin by considering the equalization of initially different ion and electron temperatures.

In the simplest case we start with flat density, zero particle flows, linearly decreasing T_e in R and flat T_i , and set all transport coefficients (or analogously only anomalous transport coefficients) to zero. The time evolution of Δt (normalized to Δt_{max}) is shown in Fig.3, as an indicator of the convergence to steady state. The exact steady state is characterized by equal temperatures, both linearly decreasing with R , no particle flow and flat density everywhere; this result is reproduced with fairly good accuracy by the code, as reported in Tab.1 (here, as in all plots, R is rescaled to R_0 and normalized to L_R , Z is rescaled to Z_0 and normalized to L_Z , ρ , T_e and T_i are normalized to their Dirichlet boundary values, and the particle fluxes are normalized to $\bar{\rho}\sqrt{T/m_i}$).

We now consider the same set of initial conditions but now with finite transport coefficients; clearly, perpendicular diffusion will lead to an exact steady state solution which is stationary, and density, electron pressure, total energy density have everywhere in Ω the value imposed at $R = R_0 + L_R$. The time variation of Δt for this case is shown in Fig.4 and the steady state obtained is summarized in Tab.2. Notice that the evolution is slower.

In all previous tests the velocity field is essentially zero everywhere at any time. We now consider as initial condition flat density, equal and flat electron and ion temperature, but an initial profile of parallel flow as given in Fig.5. The evolution of Δt in this case is given in Fig.6. In Fig.7 we give the time evolution of the parallel flow at

($R = R_0, Z = L_Z/2$): as can be expected the plasma, initially directed towards $Z = L_Z$, bounces back and forth between the two adiabatic boundaries, but in the meanwhile parallel and perpendicular viscosity dissipate momentum leading to the same exact steady state as in the previous case. The numerical steady state is summarized in Tab.3.

In a second more demanding set of tests we assumed certain spatial profiles $\mathbf{u} = \tilde{\mathbf{u}}(\mathbf{x})$ and computed analytically the sources and the boundary conditions which would make $\tilde{\mathbf{u}}$ a steady state solution of our model. The code can then be tested by using those sources as input together with the respective boundary conditions, and checking how far from $\tilde{\mathbf{u}}$ the computed steady state results are, when one starts with an initial condition far from $\tilde{\mathbf{u}}$.

In Fig.8 we summarize the tests performed, indicating the different boundary conditions used in each of them. In test A the inboard upper and lower boundaries are adiabatic. In test B Neumann boundary conditions are tested by imposing given particle parallel momentum and energy normal influxes at the inboard boundary. In test C (nonlinear) Robin conditions are tested by imposing energy outfluxes at the upper boundary. In test D, finally, the outflow contribution in the continuity equation is tested by imposing a Mach number condition on the parallel particle outflux at the upper boundary (for consistency also the energy fluxes need be nonzero); here also some limitations of the Galerkin method in the presence of strong convection and large gradients will be investigated.

In the following we will concentrate on cases A and D. In cases B and C the numerical solution converges well to the expected steady state.

The exact steady state in case A is given in Figs.9a-d and the sources required to produce it are given in Figs.10a-d. The time evolution of Δt is given in Fig.11 and the time evolution of the parallel particle flow profile is shown in Figs.12a-f. Notice, by comparing Figs.9b and 12f, that the computed steady state is fairly accurate except at the inboard boundary where the weak Robin boundary condition still allows some relaxation. The convergence of the computed solution to the exact steady state can be more quantitatively judged from Fig.13 where the time evolution of $m \delta \rho \equiv \max\{|\rho(\mathbf{x}) - \tilde{\rho}(\mathbf{x})|/\tilde{\rho}(\mathbf{x})\}$ is given.

In case D we used sources corresponding to a steady state characterized by: isothermal Mach number $M \equiv \sqrt{m_i V_{\parallel}^2 / (T_e + T_i)}$ equal to 1 at the upper boundary, parallel particle

flux uniform in R but increasing from 0 at $Z=0$ with different powers of Z , and uniform density, electron pressure and total energy density. Notice that with 10 equispaced elements in Z , $\rho = \bar{\rho} = 10^{20} \text{ m}^{-3}$, and $T_e = T_i = \bar{T}$, near the outflow boundary the mesh (electron) Peclet number $Pe \sim \frac{\Gamma_{\parallel}}{b_{\theta}} \frac{\Delta Z}{\kappa_{\parallel}^e} \approx 10$, and even with the enhanced viscosity the mesh Reynolds number $Re \sim \frac{\Gamma_{\parallel}}{b_{\theta}} \frac{\Delta Z}{\eta_0} > Pe$. Notice also that a reduction by a factor of 4 in the temperatures would lead to an increase of Pe and Re by a factor of 32.

When Γ_{\parallel} increases linearly at steady state between the lower and the upper boundary, convergence is good as expected (since the trial functions λ exactly interpolate the solution), as one can see from the time dependence of the error given in Fig.14.

When Γ_{\parallel} increases at steady state with the sixth power of Z , as shown in Fig.15, the large unresolved gradient in the solution impedes convergence as indicated in the error plot (Fig.16) and in the computed density profile at steady state (Fig.17). Since the origin of the difficulty is clearly localized in space one can improve convergence by using a mesh accumulated near the upper boundary (Figs.18-19) and further improve it by doubling the number of elements in the Z direction (Figs.20-21).

In the last test, Figs.22-23, we use the classical η_0^i (without enhancement), therefore $Re \sim \sqrt{m_i/m_e} Pe \gg Pe$ and one expects difficulties with the Galerkin method even with an accumulated mesh with 20 elements in Z . In order for the GMRES iterations to converge to the prescribed (10^{-12}) tolerance we needed to increase from 5 to, e.g., 20 the dimension of the Krylov space where the minimization of the residual is performed; furthermore, whenever the GMRES iteration does not converge the step is rejected and Δt_{max} is set equal to the Δt at the previous step.

More complex tests relevant to a typical SOL (see, e.g., [4]) will be reported in the future.

5. Conclusions

We have developed a finite element code which can be used as a basis for fluid modeling of the scrape-off layer. From the point of view of the fluid plasma several of the essential physics ingredients are included in the model: classical transport is assumed along magnetic field lines, anomalous transport perpendicular to magnetic surfaces, and different ion and electron temperatures are allowed. In a rather extensive set of test cases in simple geometry the code has been shown to work.

More realistic SOL sources, describing the interaction with recycling neutrals, and boundary conditions, related, e.g., to the Debye sheath at the target, are being implemented. This should also indicate if Galerkin with a suitably chosen mesh is enough - in SOL modeling problems the steady state location of "difficult" regions is essentially known *a priori* -, or if some additional numerical dissipation is required in the region of strong convection and large gradients expected near the target. Also a general target and magnetic geometry should be tested, but this is for the moment impossible with the present version of the unstructured mesh generator (see [4]).

Diamagnetic flows, electric currents, impurities, which have been neglected for the time being, will be the subject of subsequent work.

Acknowledgements

I wish to thank Prof.K.Lackner, Dr.J.Neuhauser, Prof.C.Canuto (Torino) and Dr. A.Russo (Pavia) for several useful discussions, and again J.N. for a careful reading of the manuscript. This work was partially financially supported by a EURATOM Mobility contract and by A.S.S.T.P. Torino.

References

- [1] B.J.Braams, NET Report EUR-FU/XII-80/87/68 (1987).
- [2] R.Zanino and W.Schneider, *Contrib. Plasma Phys.* 30 (1990) 127.
- [3] R.Zanino, *J. Nucl. Mater.* 176 & 177 (1990) 750.
- [4] R.Zanino, Rapporto Politecnico di Torino PT DE IN 260 (1991).
- [5] S.I.Braginskii, in *Reviews of Plasma Physics*, M.A.Leontovich ed.,
(Consultants Bureau, NY, 1965) Vol.1, 205.
- [6] R.Zanino, Max-Planck-Institut Report IPP 5/38 (1990).
- [7] W.M.Stacey, Jr. and D.J.Sigmar, *Phys. Fluids* 28 (1985) 2800.

Acknowledgements

I wish to thank Prof. H. Lackner, Dr. J. Neuhauser, Prof. C. Gennaro (Torino) and Dr. A. Russo (Pavia) for several useful discussions, and again J.N. for a careful reading of the manuscript. This work was partially financially supported by a EURATOM-Mobility contract and by A.S.T.P. Torino.

Figure captions

Fig.1

Computational domain.

Fig.2

Simplified computational domain.

Fig.3a

Adaptive Δt evolution for $T_e(R, Z, t = 0) = 2 - (R - R_0)/L_R$, $T_i(R, Z, t = 0) = \rho(R, Z, t = 0) = 1$, $\Gamma_{||}(R, Z, t = 0) = \Gamma_{\psi}(R, Z, t = 0) = 0$. No diffusive transport.

Fig.4

As Fig.3 but with diffusive transport.

Figs.5

$\Gamma_{||}(R, Z, t = 0)$.

Fig.6

Δt evolution with initial condition as in Fig.5.

Fig.7

Time evolution of $\Gamma_{||}(R_0, L_Z/2)$.

Fig.8

Summary of boundary conditions for tests with sources.

Fig.9

Exact steady state for test A: (a) ρ , (b) $\Gamma_{||}$, (c) p_e , (d) \mathcal{E} .

Fig.10

Sources for test A: (a) S^m , (b) $\mathbf{b} \cdot \mathbf{S}^p$, (c) S_e^E , (d) S_i^E .

Fig.11

Δt evolution for test A.

Fig.12

Evolution of $\Gamma_{||}(R, Z)$ for test A:

after (a) 20, (b) 40, (c) 60, (d) 80, (e) 100 steps; (f) steady state.

Fig.13

Evolution of the maximum relative error in ρ for test A.

Fig.14

Evolution of the maximum relative error in ρ for test D.

$\Gamma_{||}(R, Z) = Z/L_Z$ at steady state.

Fig.15

$\Gamma_{||}(R, Z) = (Z/L_Z)^6$.

Fig.16

Evolution of the maximum relative error in ρ for test D with $\Gamma_{||}$ at steady state as in Fig.15. Equidistant mesh with 10 elements in Z.

Fig.17

$\rho(R, Z)$ at steady state corresponding to Fig.16.

Fig.18

As Fig.16 but with accumulated mesh.

Fig.19

$\rho(R, Z)$ at steady state corresponding to Fig.18.

Fig.20

As Fig.18 but with 20 elements in Z.

Fig.21

$\rho(R, Z)$ at steady state corresponding to Fig.20.

Fig.22

Δt evolution for test D with $\Gamma_{||}$ at steady state as in Fig.15.

η_0^i not artificially enhanced.

Fig.23

Evolution of the maximum relative error in ρ corresponding to Fig.22.

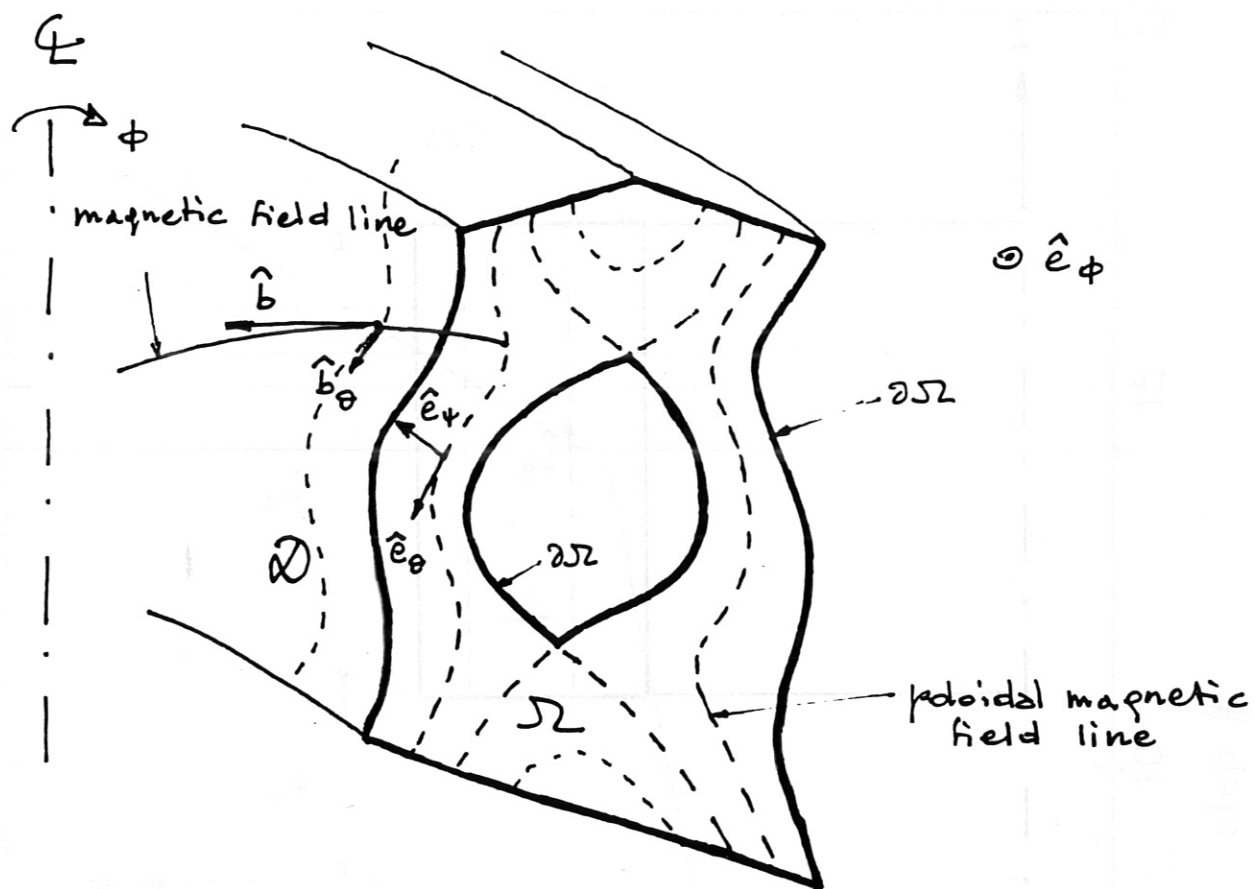


Fig. 1

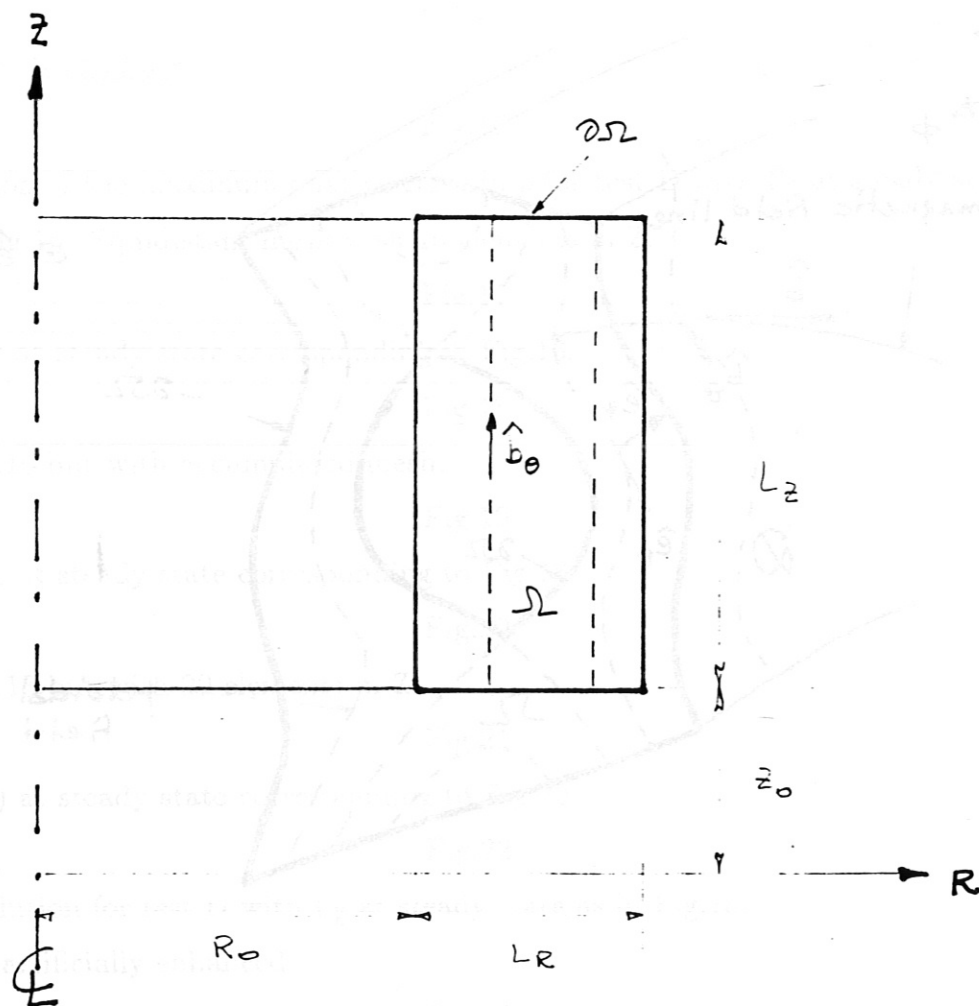


Fig. 2

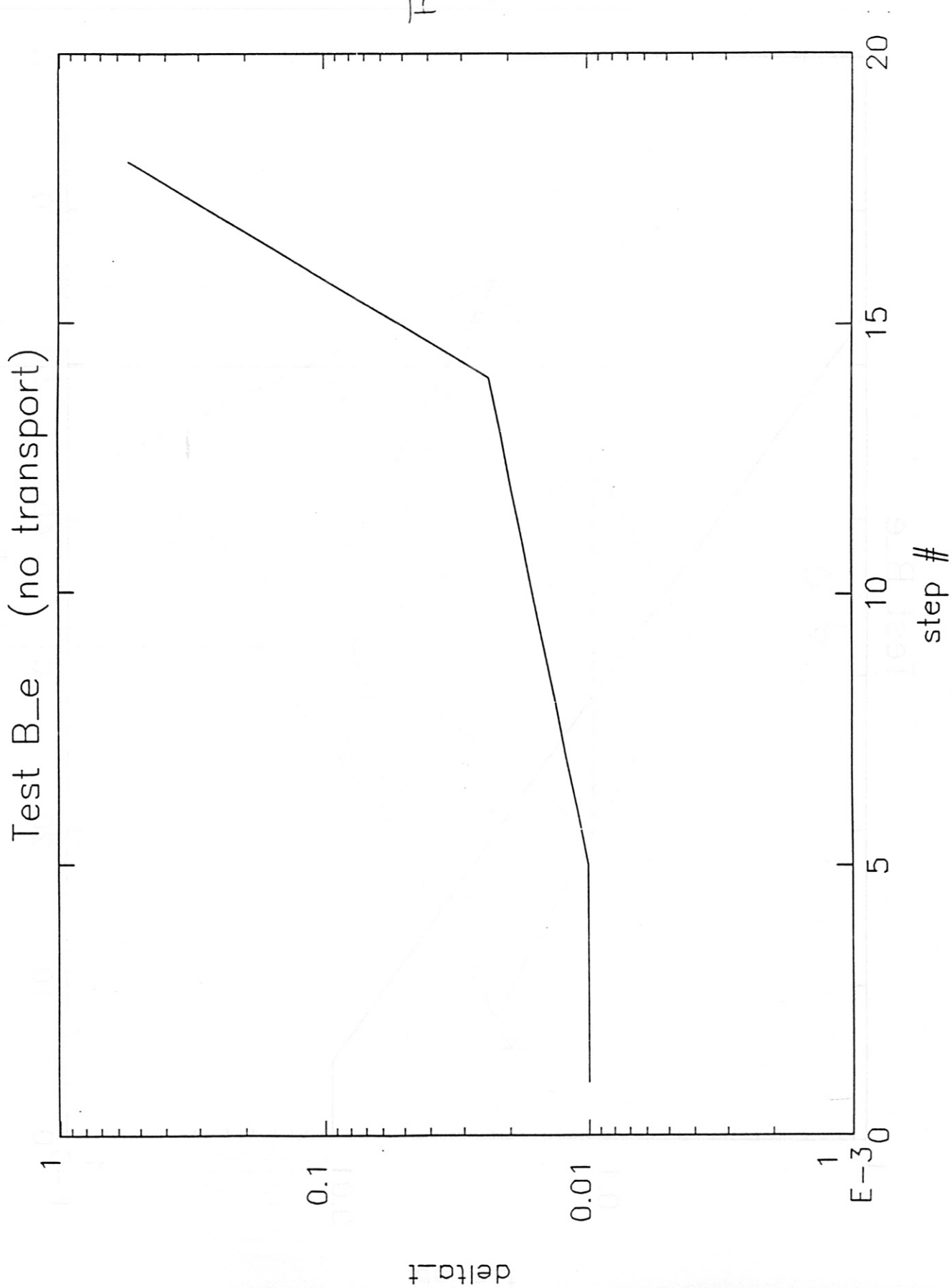


Fig. 3

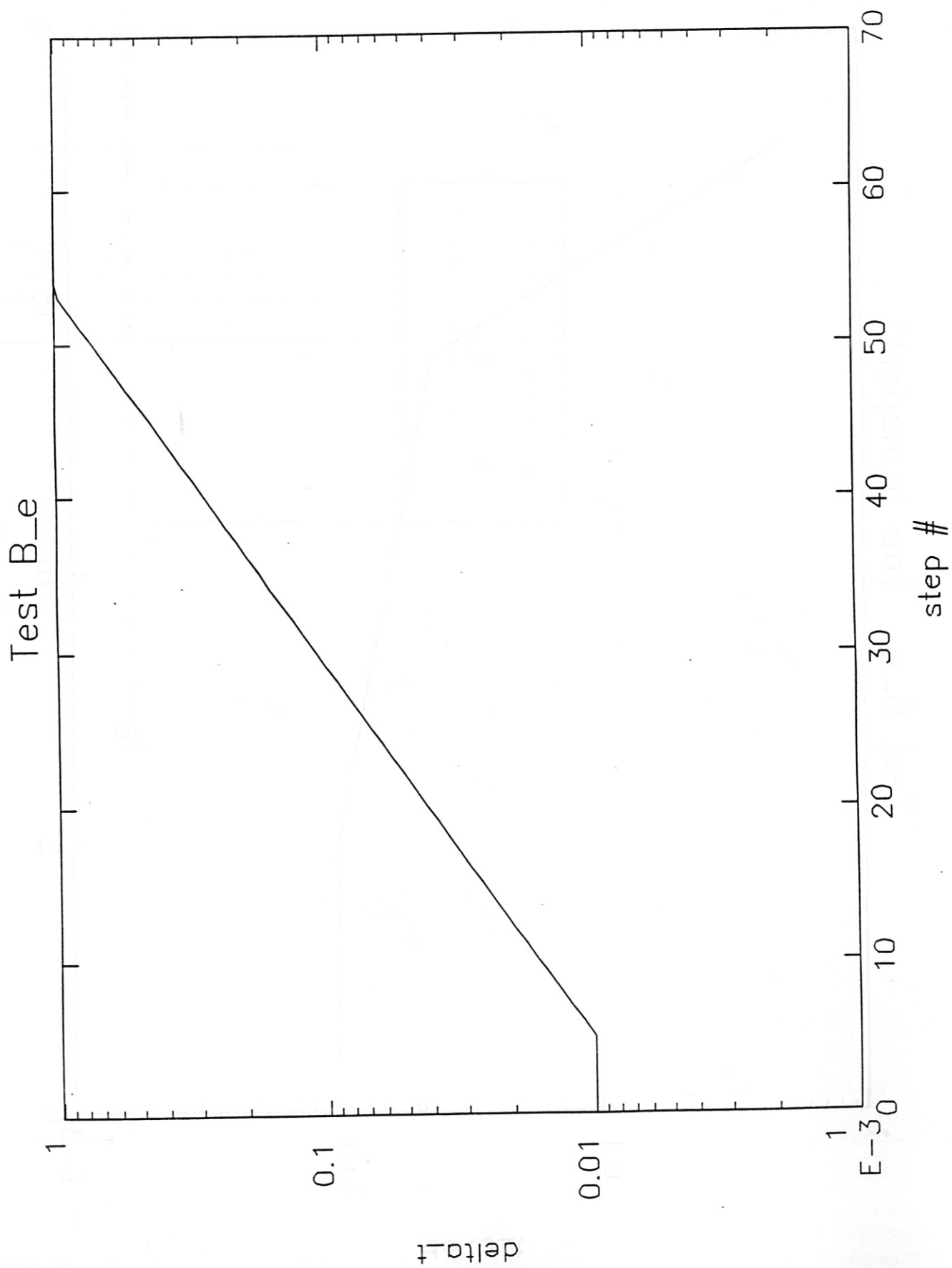


Fig. 4

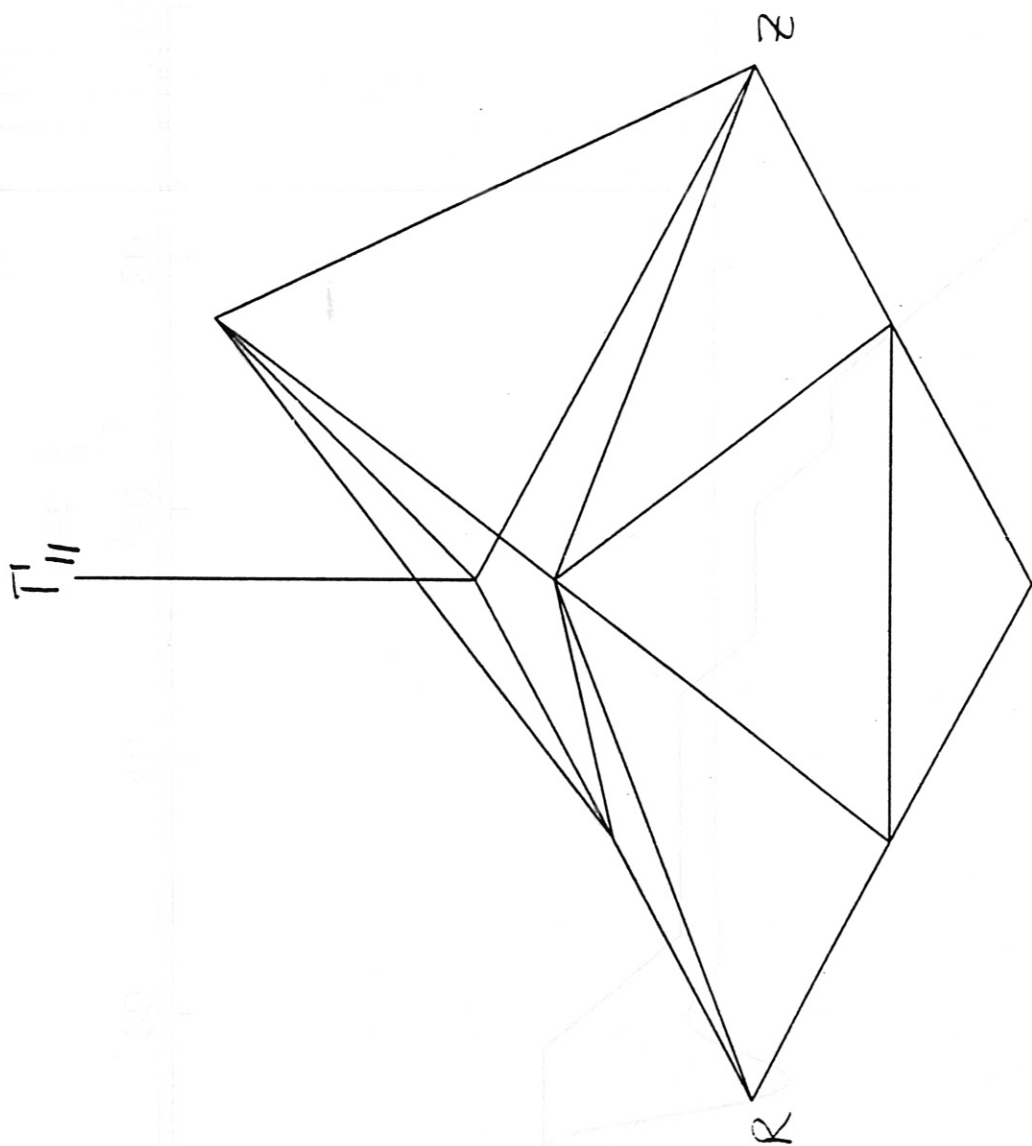


Fig. 5

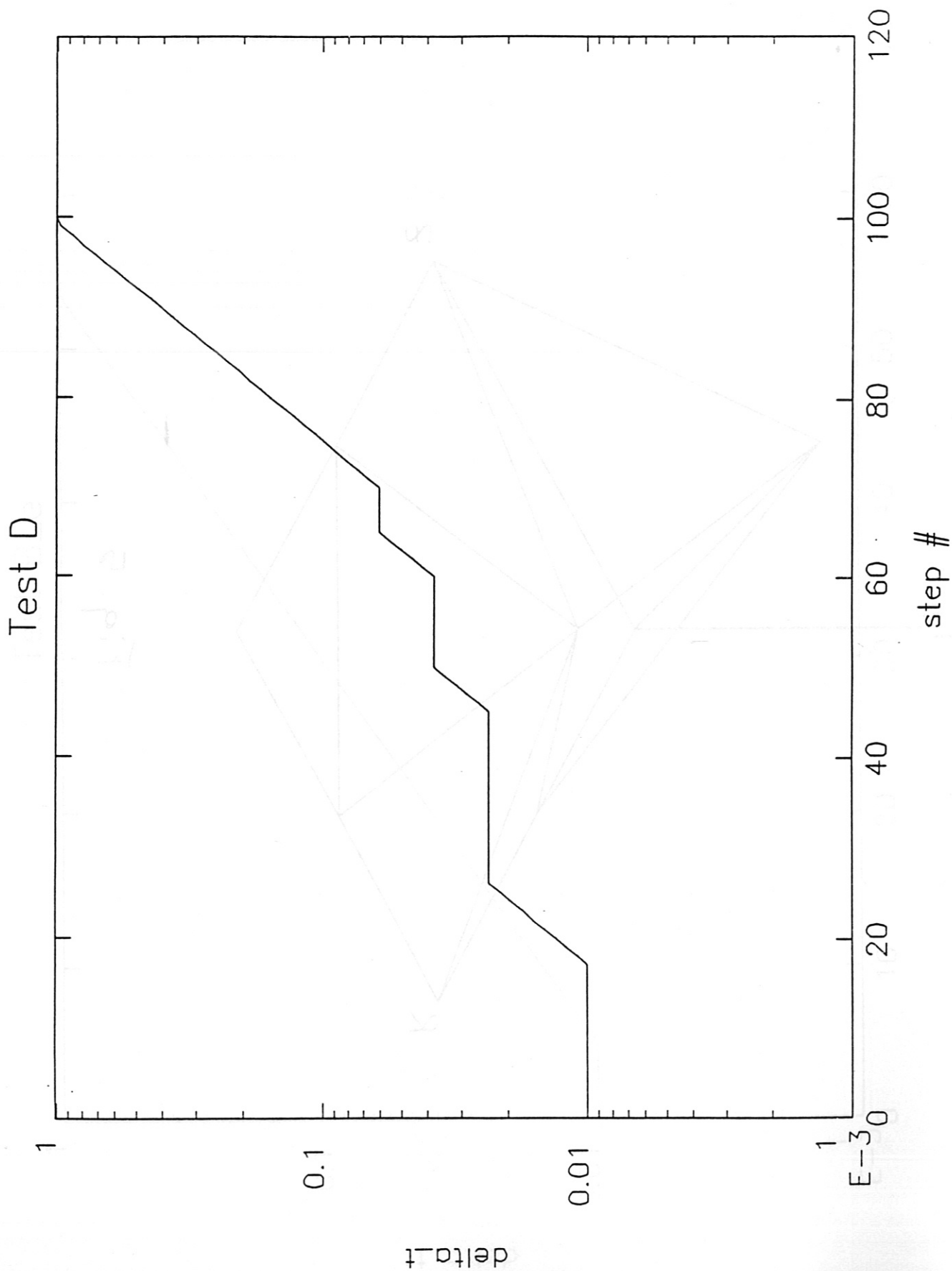


Fig. 6

Test D

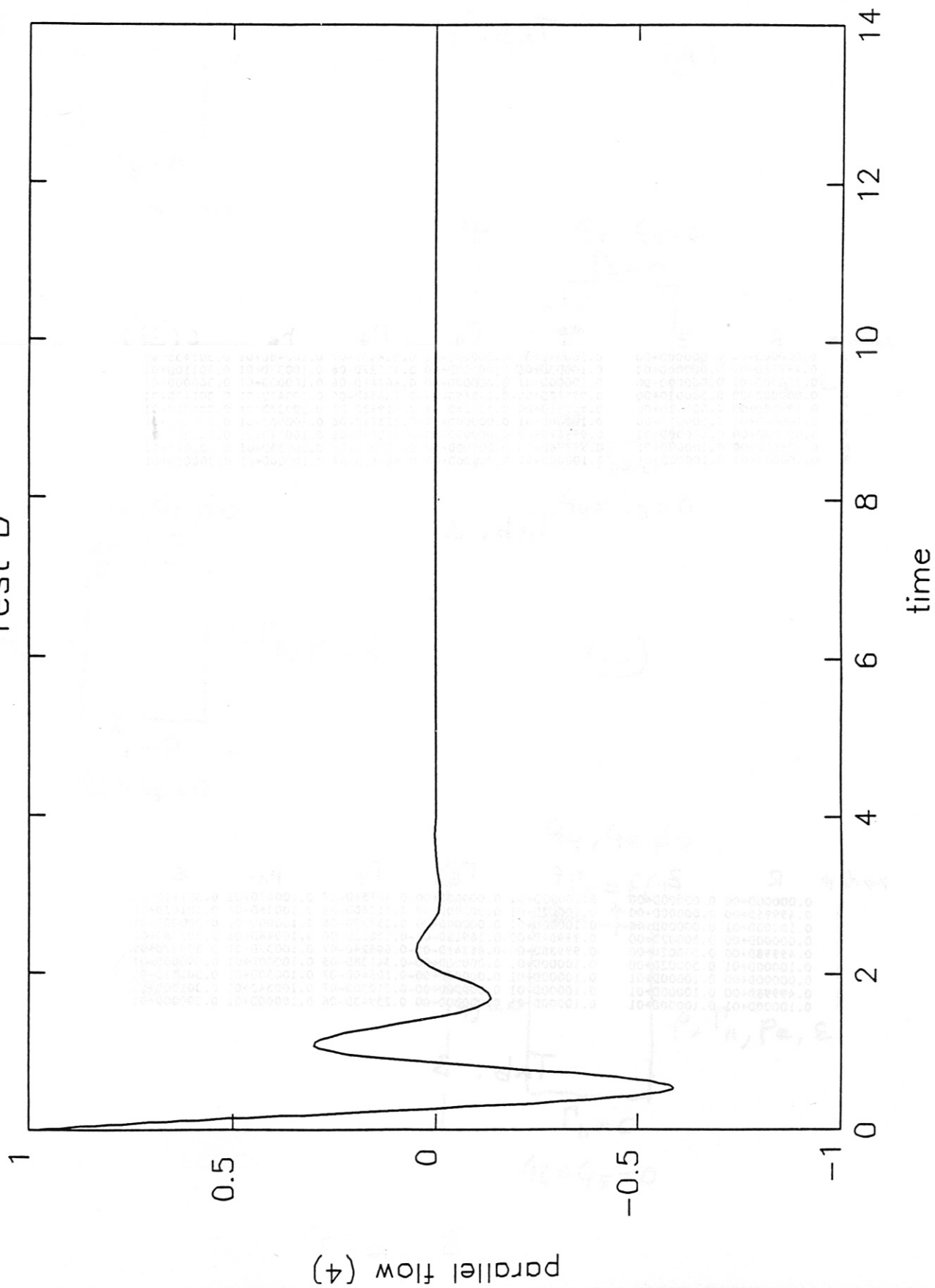


Fig. 7

node #	R	Z	ρ	Γ_{II}	Γ_{ψ}	p_e	ε
1	0.00000D+00	0.00000D+00	0.10000D+01	0.00000D+00	0.00000D+00	0.15000D+01	0.45000D+01
2	0.49998D+00	0.00000D+00	0.10000D+01	0.00000D+00	0.00000D+00	0.12500D+01	0.37500D+01
3	0.10000D+01	0.00000D+00	0.10000D+01	0.00000D+00	0.00000D+00	0.10000D+01	0.30000D+01
4	0.00000D+00	0.50002D+00	0.10000D+01	0.59999D-10	0.00000D+00	0.15000D+01	0.45000D+01
5	0.49998D+00	0.50002D+00	0.10000D+01	-0.55759D-10	0.00000D+00	0.12500D+01	0.37500D+01
6	0.10000D+01	0.50002D+00	0.10000D+01	0.00000D+00	0.00000D+00	0.10000D+01	0.30000D+01
7	0.00000D+00	0.10000D+01	0.10000D+01	0.00000D+00	0.00000D+00	0.15000D+01	0.45000D+01
8	0.49998D+00	0.10000D+01	0.10000D+01	0.00000D+00	0.00000D+00	0.12500D+01	0.37500D+01
9	0.10000D+01	0.10000D+01	0.10000D+01	0.00000D+00	0.00000D+00	0.10000D+01	0.30000D+01

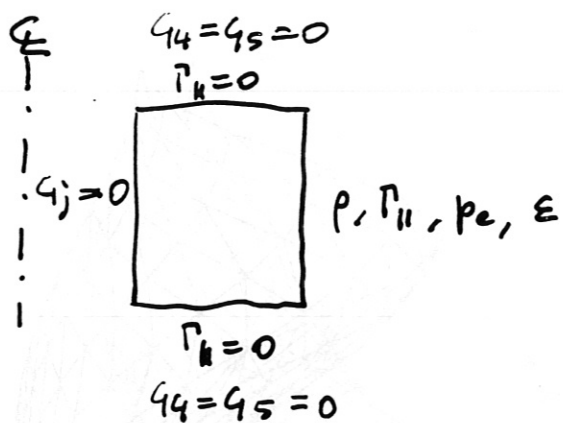
Tab. 1

node #	R	Z	ρ	Γ_{II}	Γ_{ψ}	p_e	ε
1	0.00000D+00	0.00000D+00	0.10004D+01	0.00000D+00	0.52885D-07	0.10048D+01	0.30145D+01
2	0.49998D+00	0.00000D+00	0.10003D+01	0.00000D+00	0.43527D-06	0.10037D+01	0.30110D+01
3	0.10000D+01	0.00000D+00	0.10000D+01	0.00000D+00	0.46741D-06	0.10000D+01	0.30000D+01
4	0.00000D+00	0.50002D+00	0.99988D+00	-0.14849D-04	-0.13654D-06	0.10047D+01	0.30142D+01
5	0.49998D+00	0.50002D+00	0.99991D+00	0.55724D-06	-0.11942D-07	0.10033D+01	0.30100D+01
6	0.10000D+01	0.50002D+00	0.10000D+01	0.00000D+00	-0.32261D-06	0.10000D+01	0.30000D+01
7	0.00000D+00	0.10000D+01	0.99987D+00	0.00000D+00	-0.14319D-06	0.10051D+01	0.30155D+01
8	0.49998D+00	0.10000D+01	0.99996D+00	0.00000D+00	-0.15998D-06	0.10035D+01	0.30104D+01
9	0.10000D+01	0.10000D+01	0.10000D+01	0.00000D+00	0.66961D-07	0.10000D+01	0.30000D+01

Tab. 2

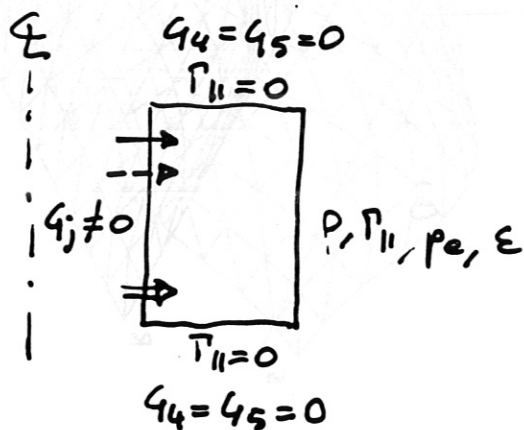
node #	R	Z	ρ	Γ_{II}	Γ_{ψ}	p_e	ε
1	0.00000D+00	0.00000D+00	0.10003D+01	0.00000D+00	0.40754D-07	0.10047D+01	0.30141D+01
2	0.49998D+00	0.00000D+00	0.10002D+01	0.00000D+00	0.31240D-06	0.10036D+01	0.30107D+01
3	0.10000D+01	0.00000D+00	0.10000D+01	0.00000D+00	0.25723D-06	0.10000D+01	0.30000D+01
4	0.00000D+00	0.50002D+00	0.99984D+00	-0.16918D-04	-0.15863D-06	0.10046D+01	0.30138D+01
5	0.49998D+00	0.50002D+00	0.99988D+00	-0.66241D-05	-0.68824D-07	0.10032D+01	0.30097D+01
6	0.10000D+01	0.50002D+00	0.10000D+01	0.00000D+00	-0.34138D-06	0.10000D+01	0.30000D+01
7	0.00000D+00	0.10000D+01	0.10000D+01	0.00000D+00	-0.10640D-07	0.10050D+01	0.30151D+01
8	0.49998D+00	0.10000D+01	0.10000D+01	0.00000D+00	-0.51030D-07	0.10034D+01	0.30100D+01
9	0.10000D+01	0.10000D+01	0.10000D+01	0.00000D+00	0.25943D-06	0.10000D+01	0.30000D+01

Tab. 3

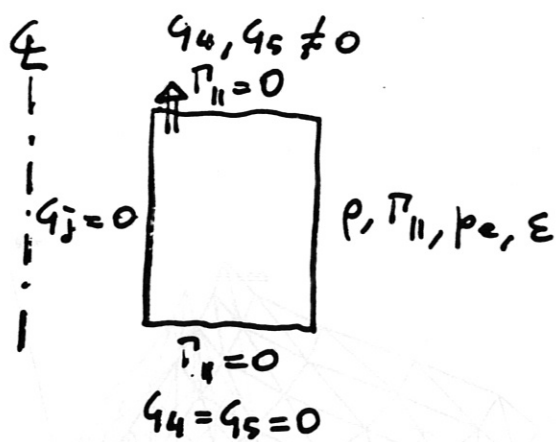


(A)

(B)



(C)



(D)

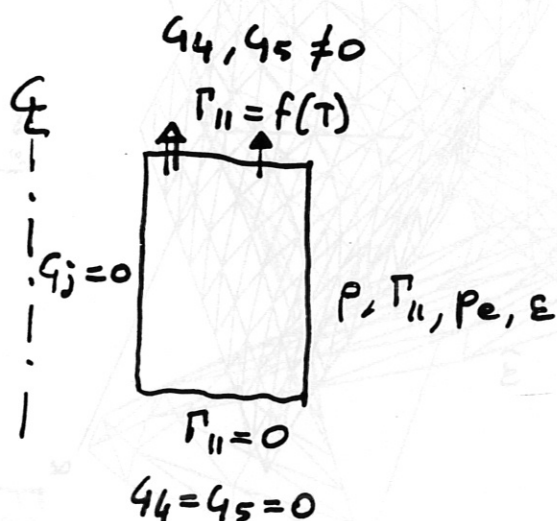
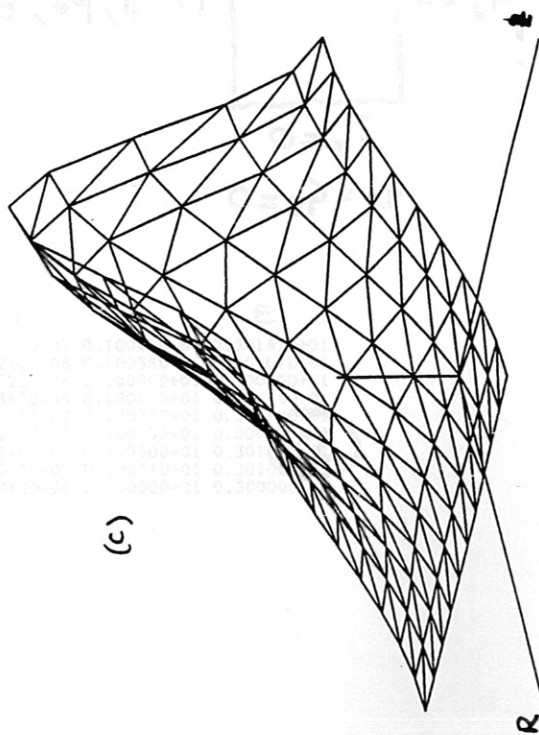
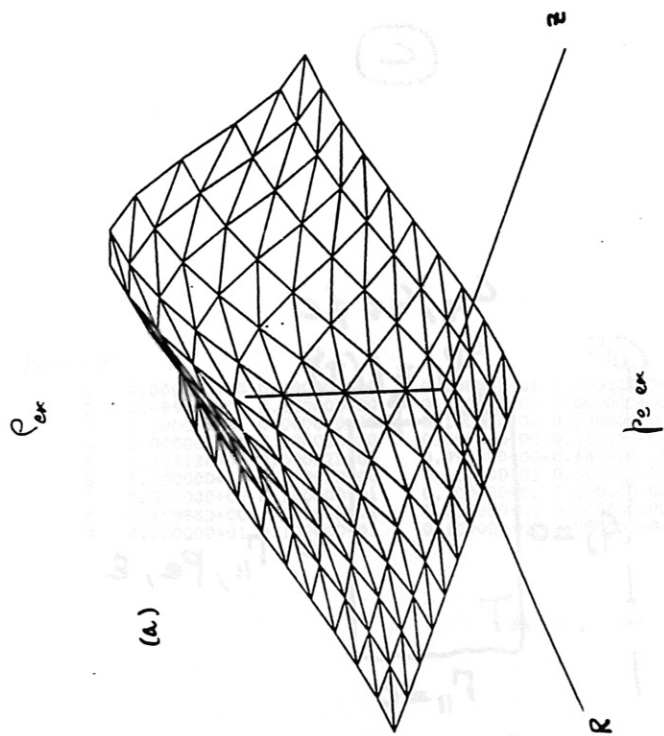
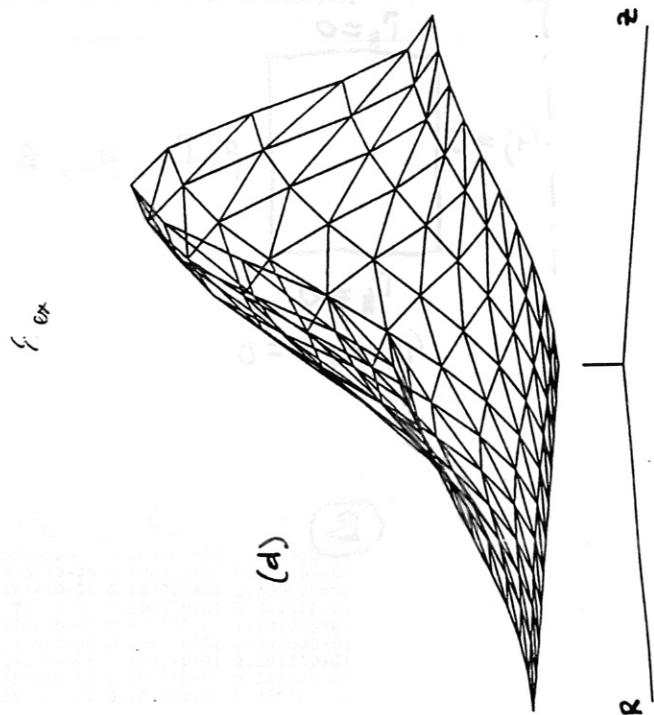
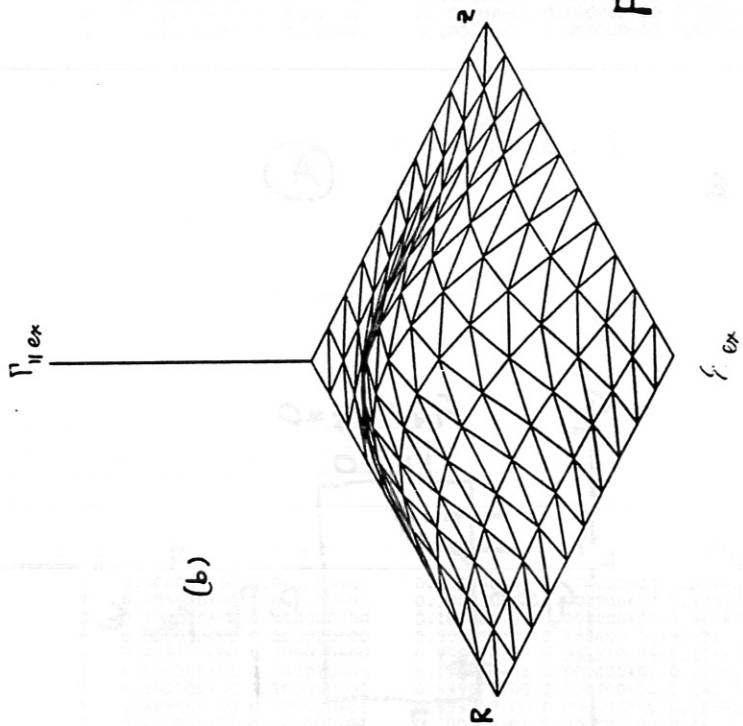


Fig. 8

Fig. 9



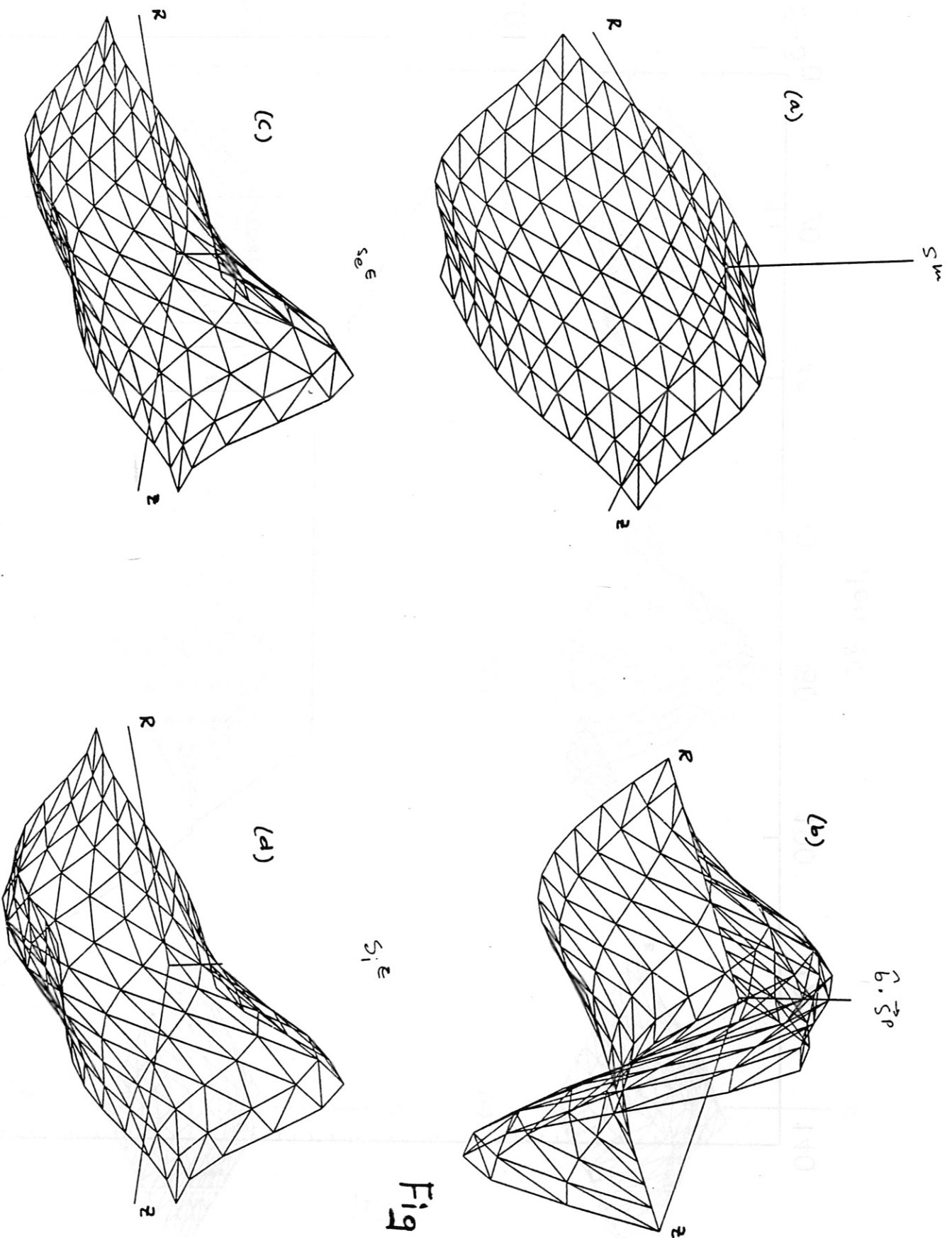
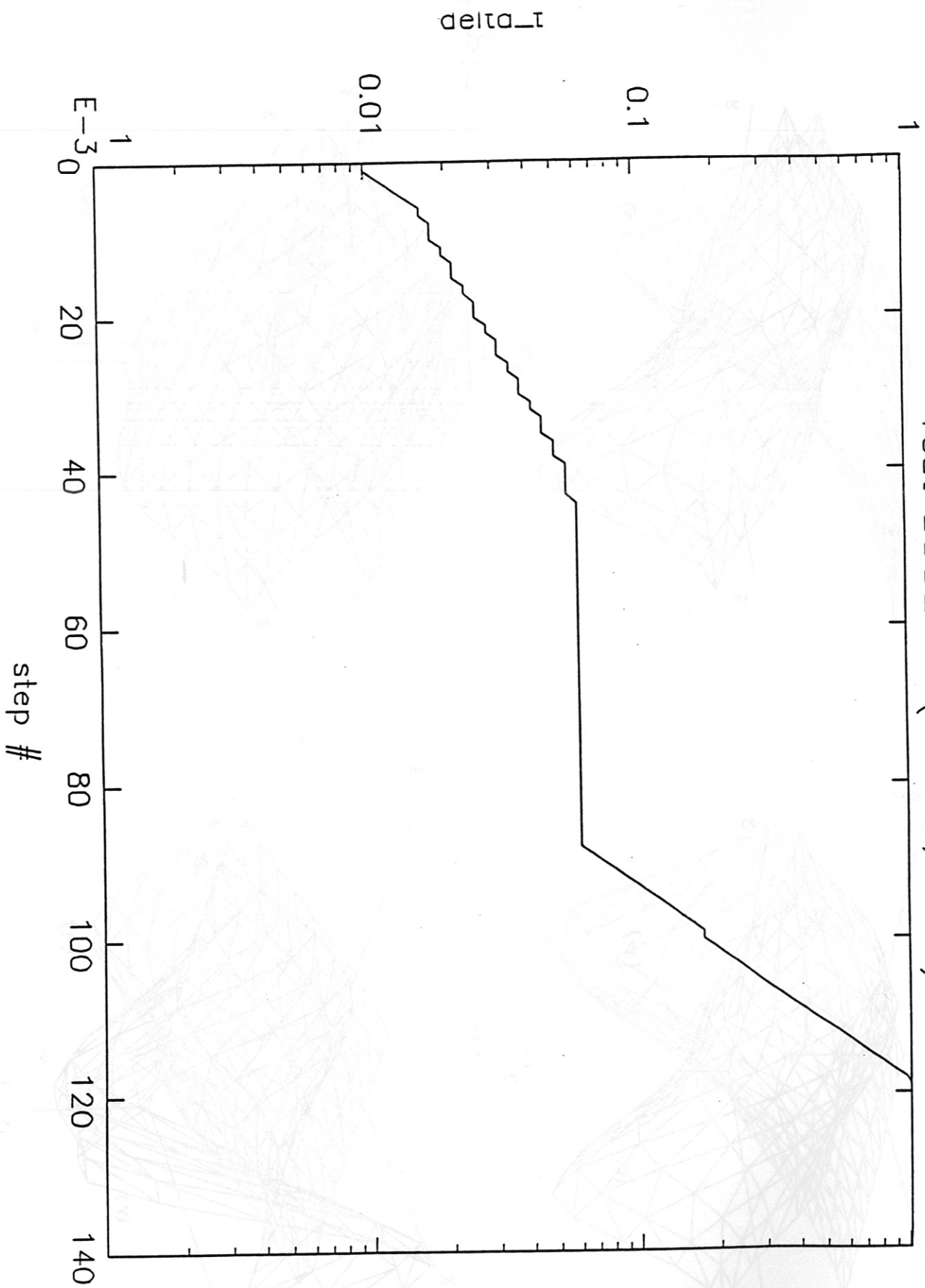


Fig. 10

Test SOUEXA (in=flat, FULL)



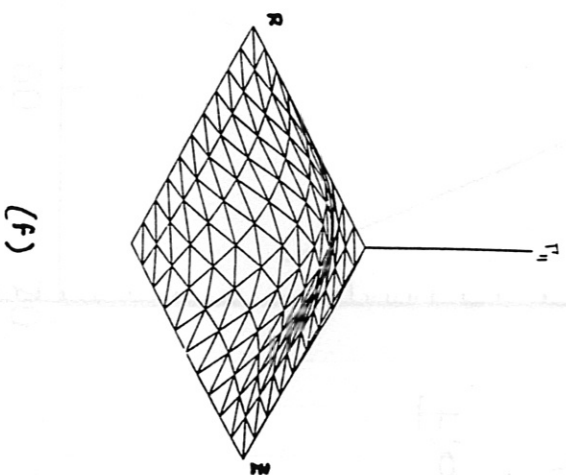
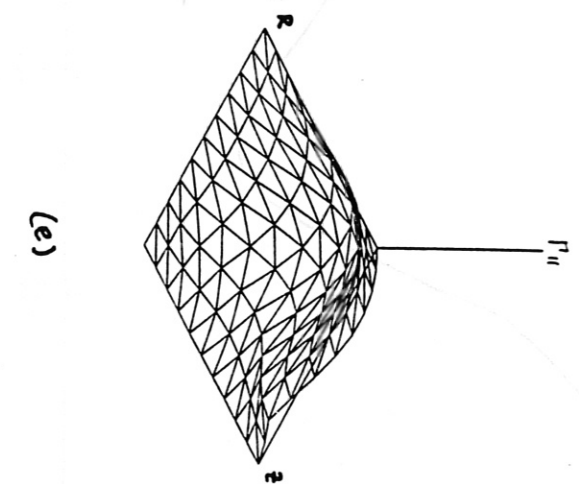
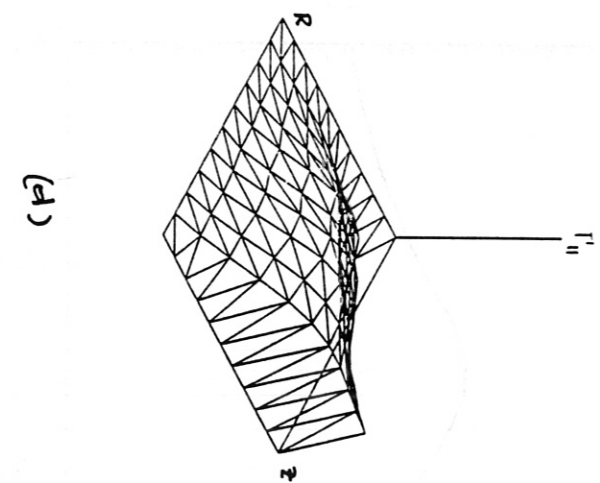
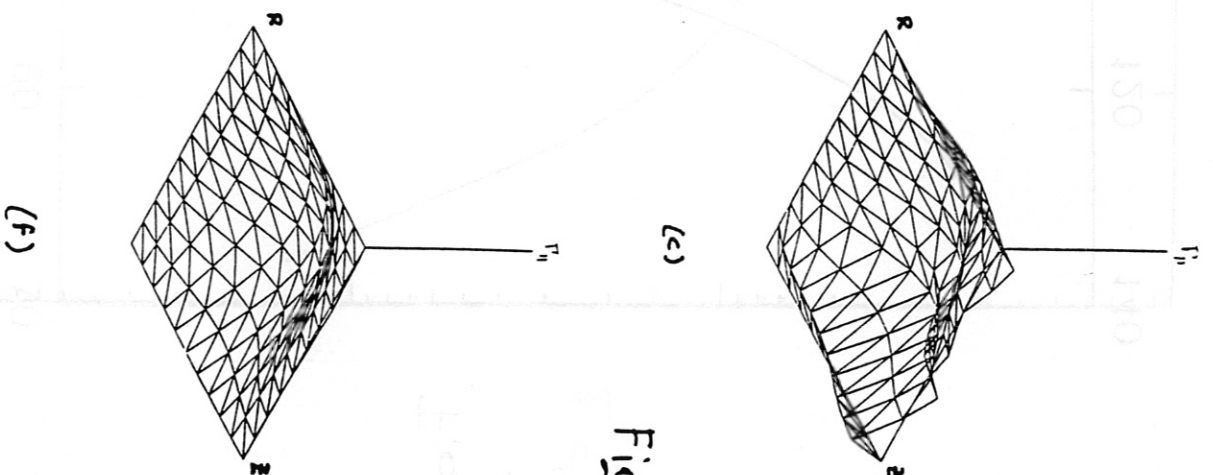
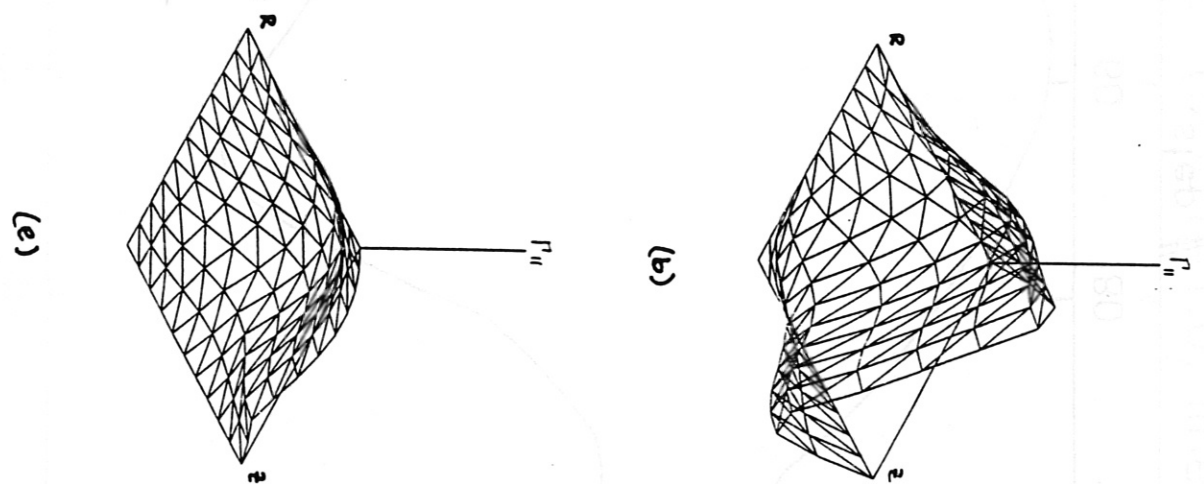
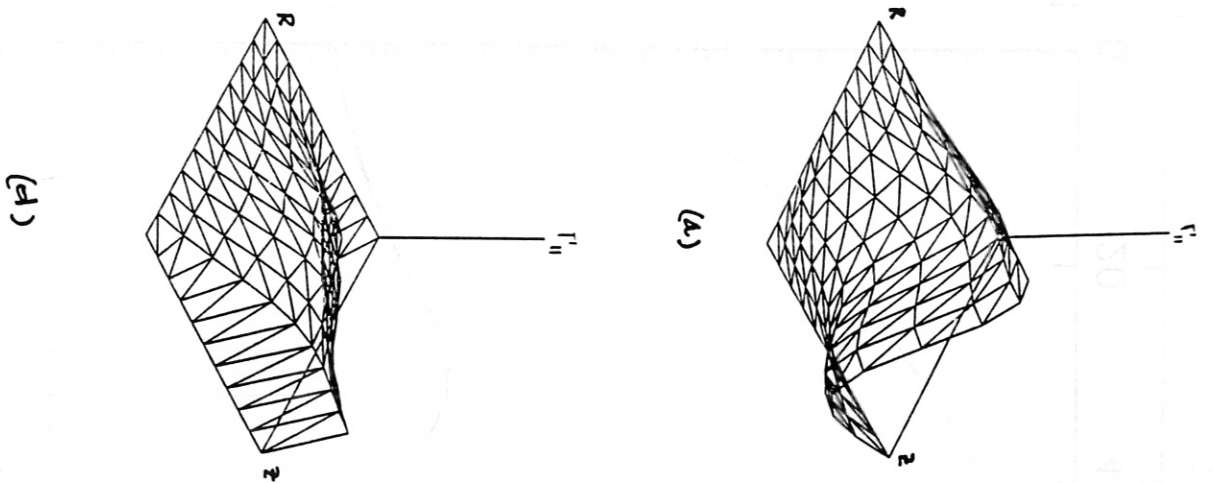


Fig. 12

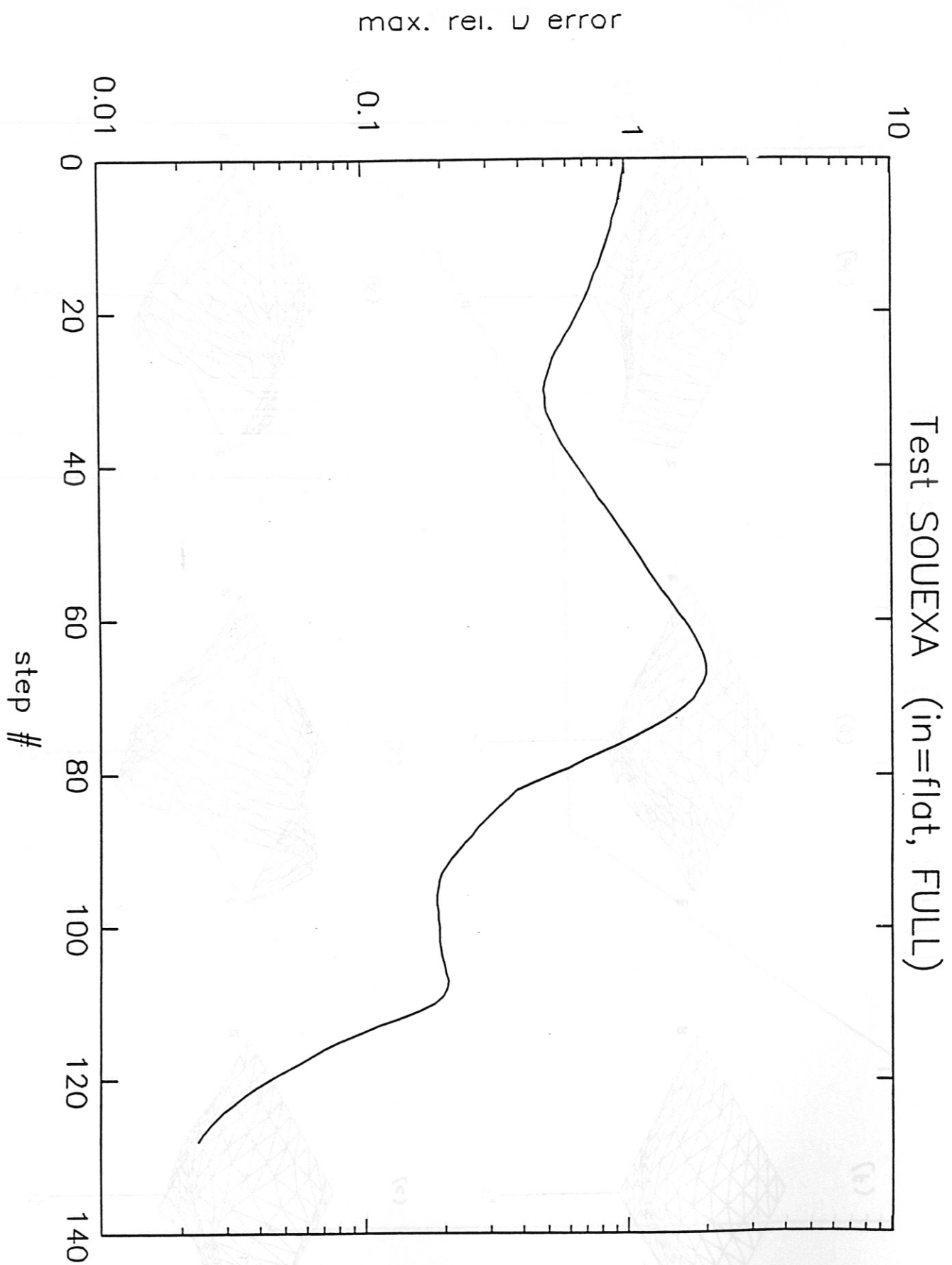


Fig. 13

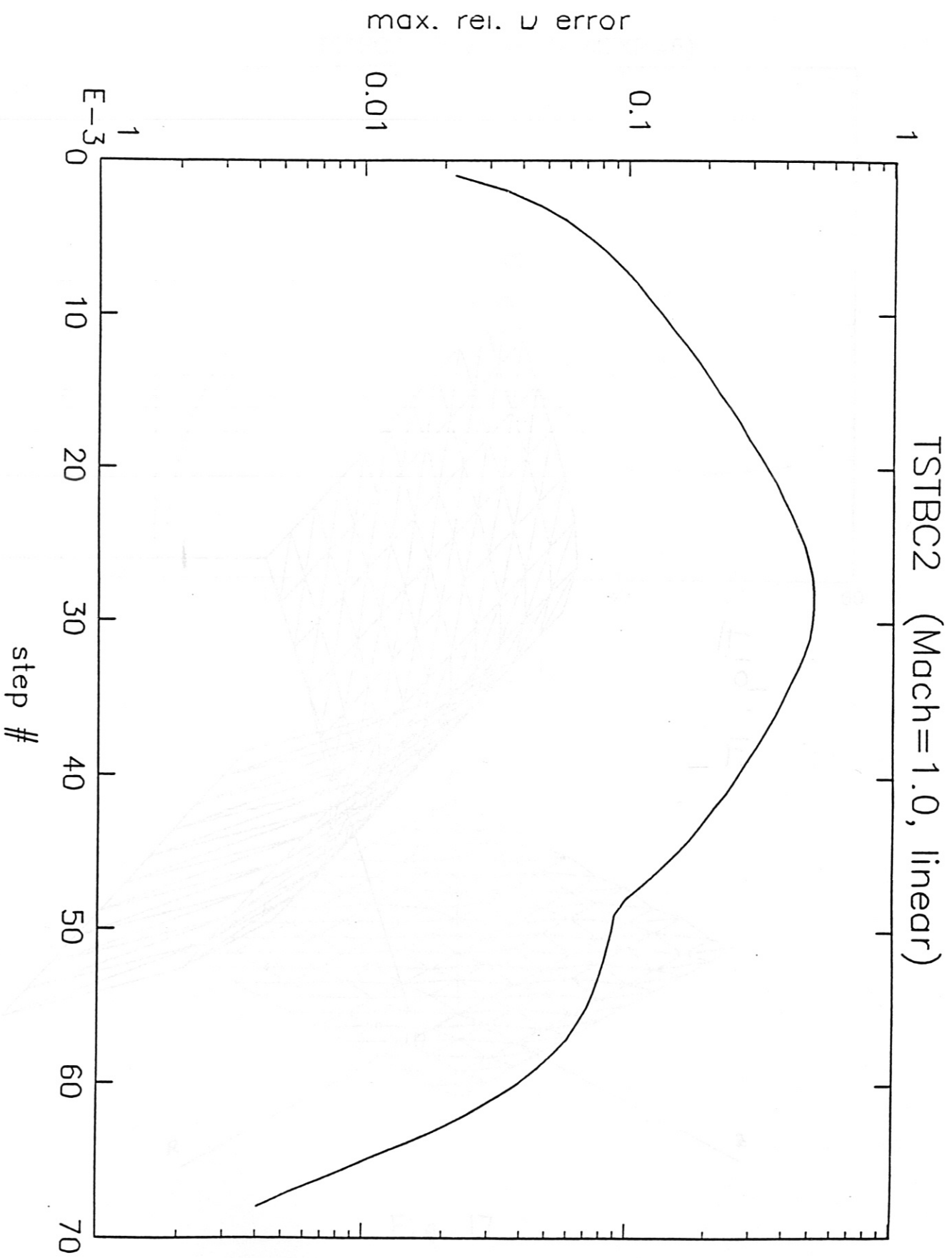


Fig. 14

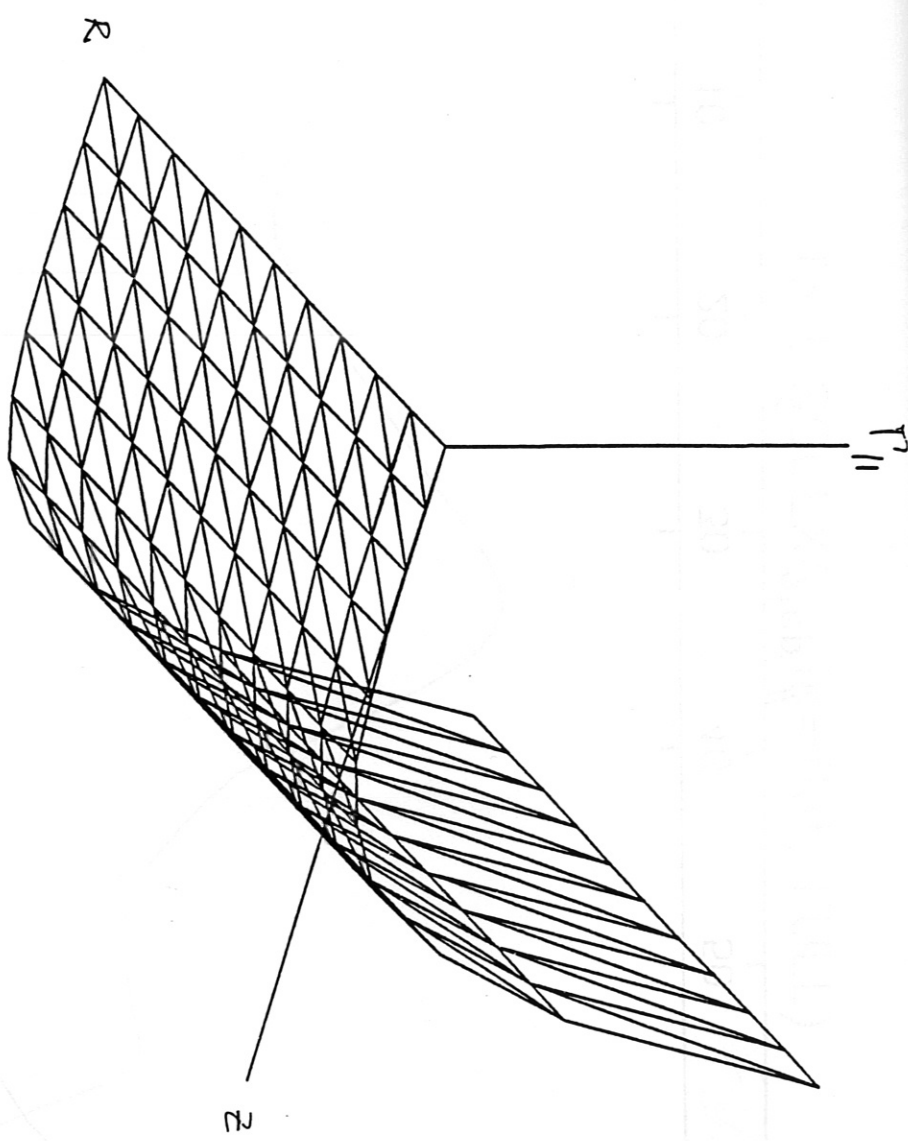


Fig. 15

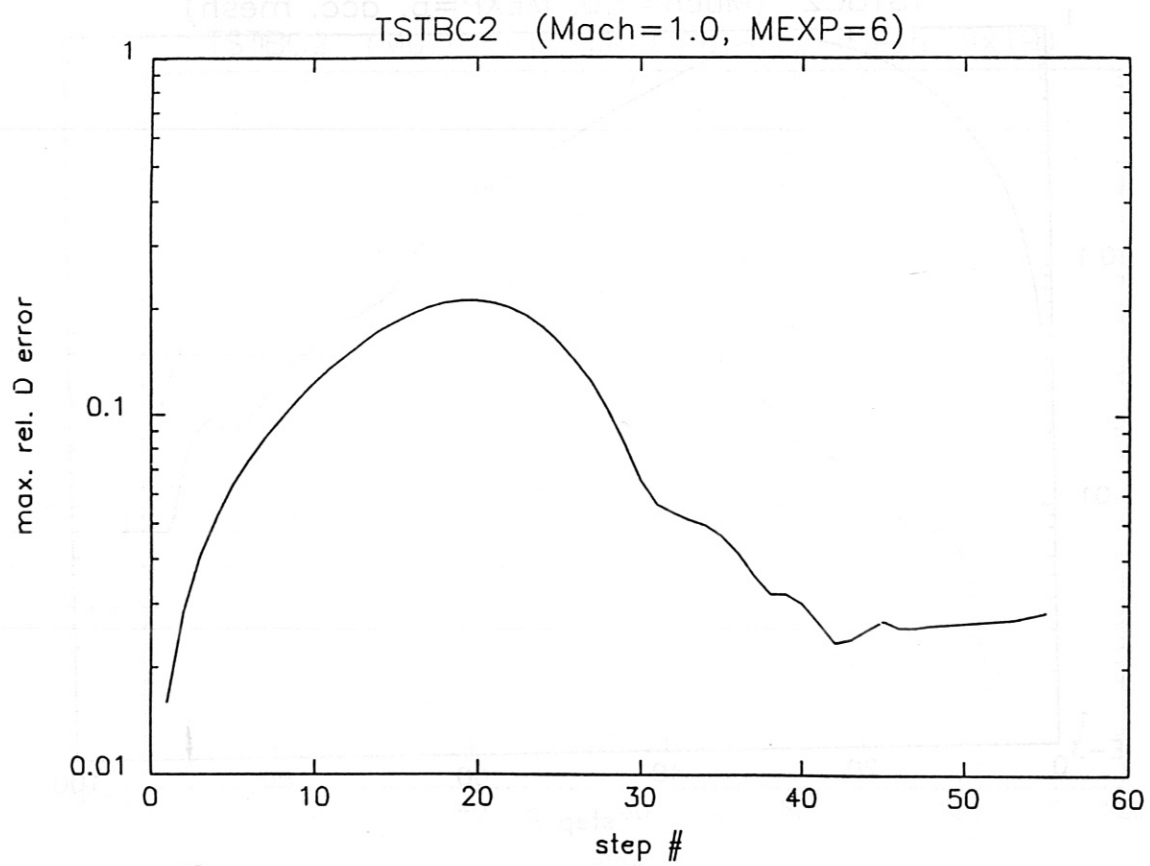


Fig. 16

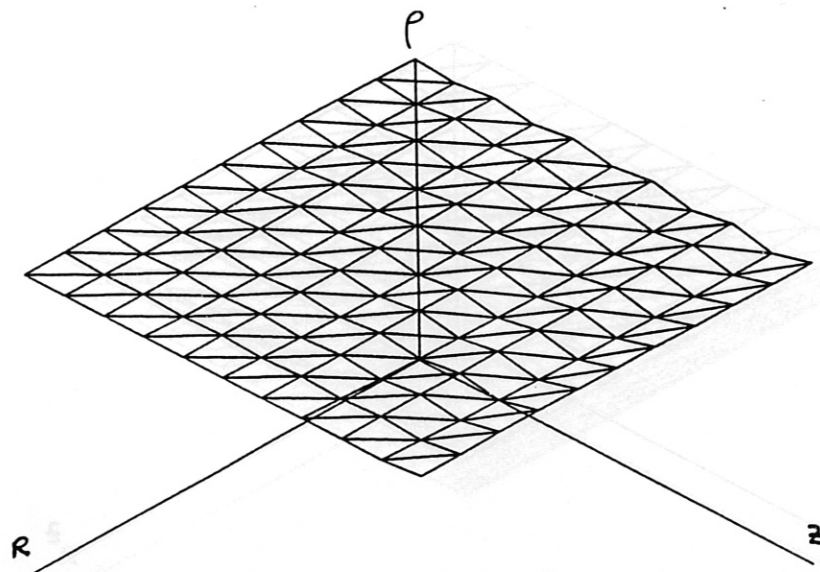


Fig. 17

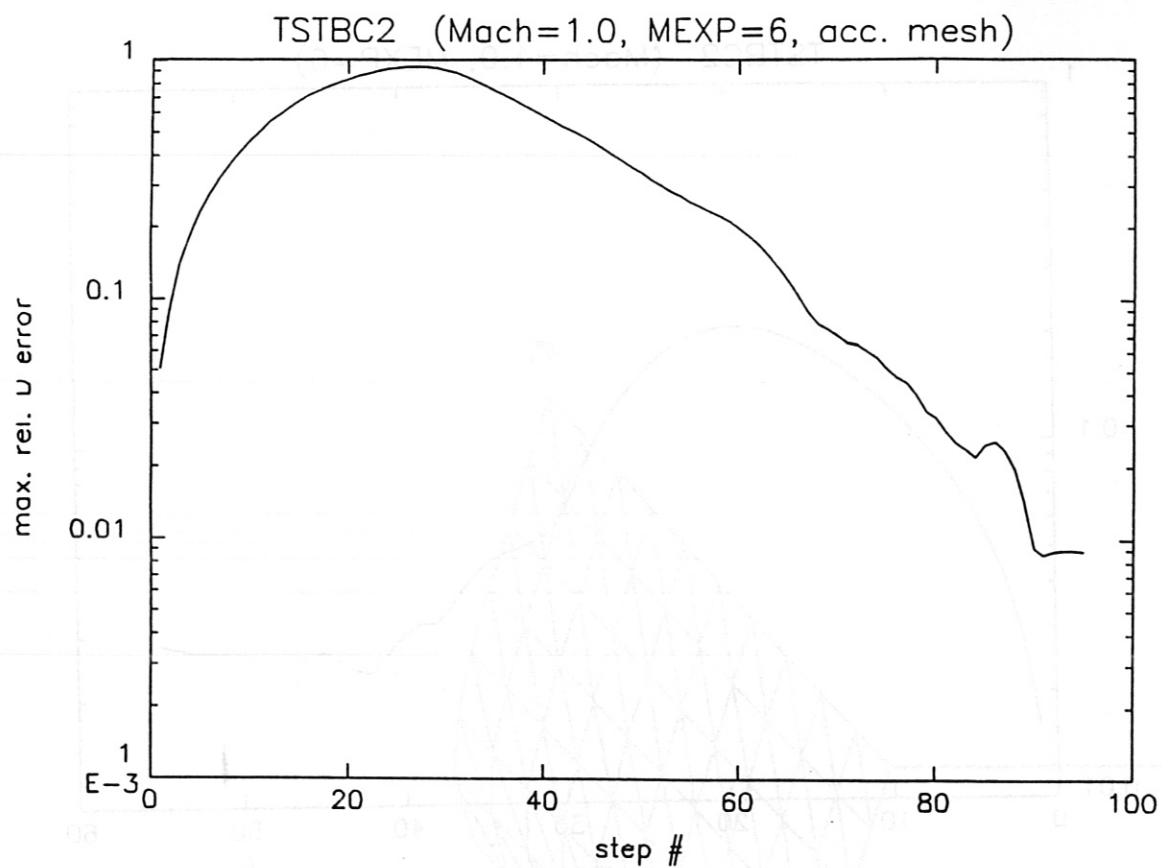


Fig. 18

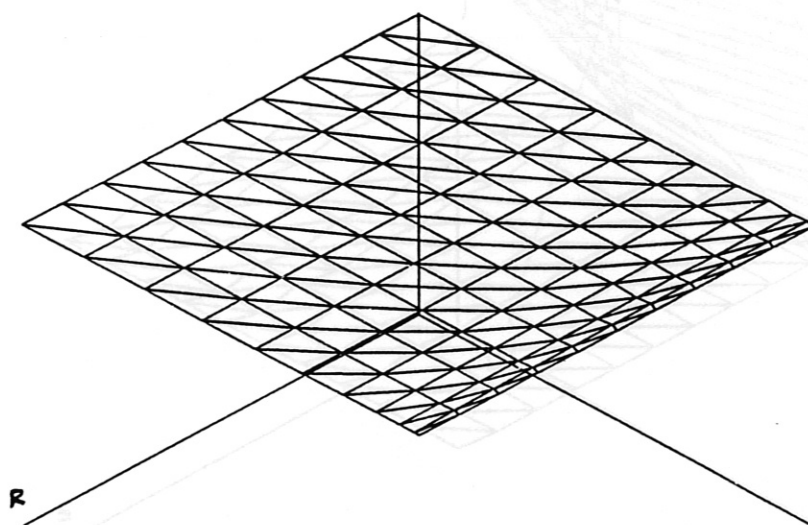


Fig. 19

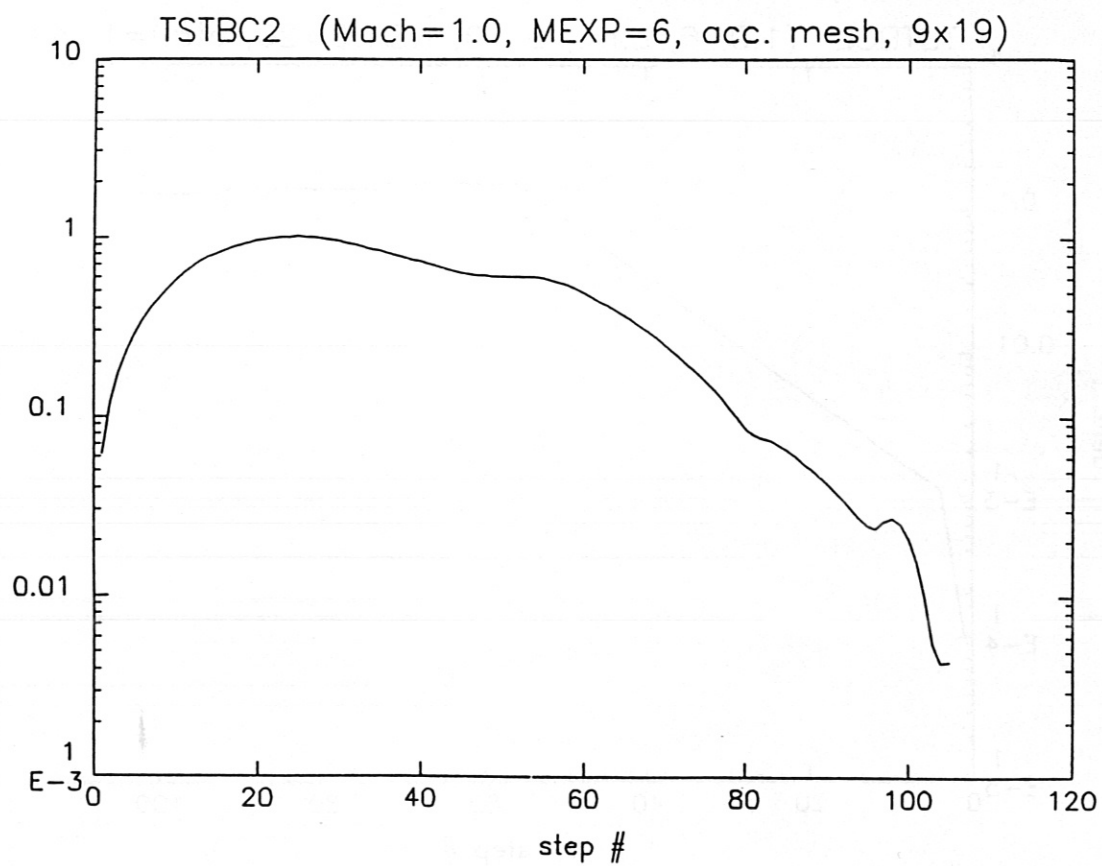


Fig. 20

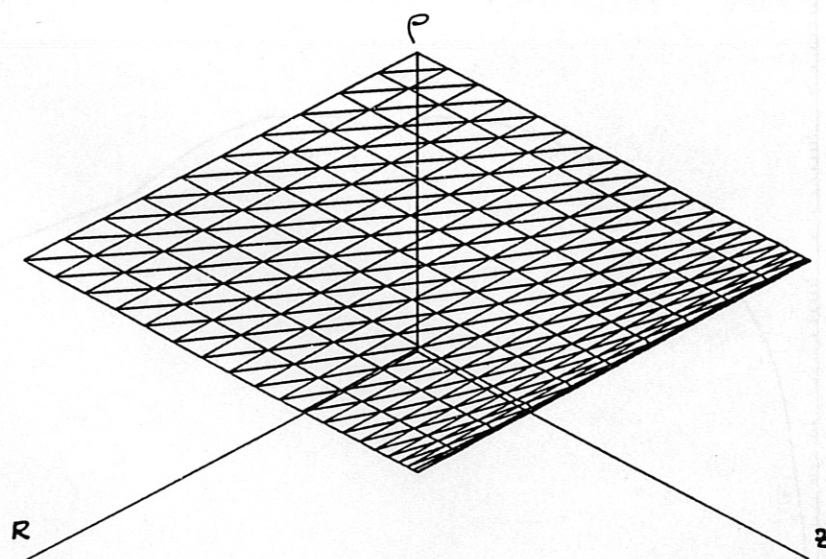


Fig. 21

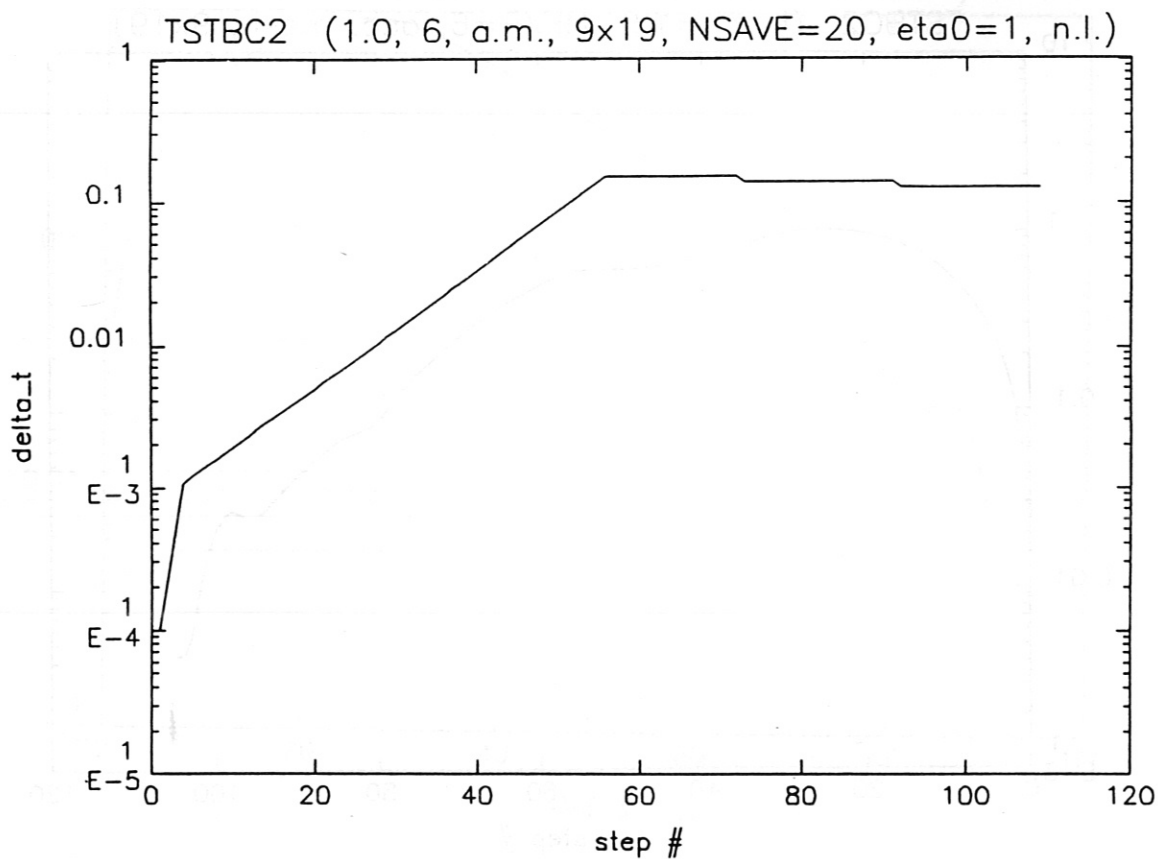


Fig. 22

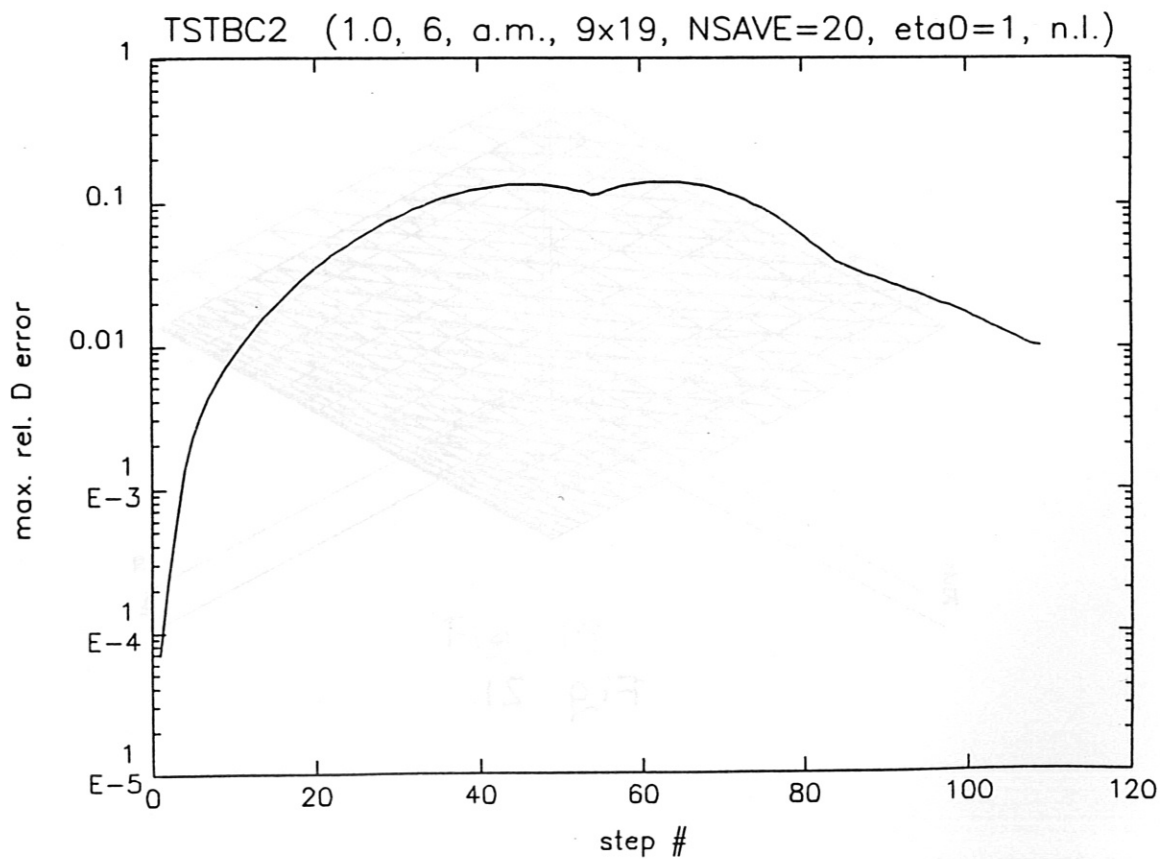


Fig. 23